Environmental Science Processes & Impacts

ROYAL SOCIETY OF CHEMISTRY

PAPER

View Article Online
View Journal | View Issue

Open Access Article. Published on 03 ottobre 2022. Downloaded on 15/09/2024 20:54:19.
This article is licensed under a Creative Commons Attribution 3.0 Unported Licence.

Check for updates

Cite this: *Environ. Sci.: Processes Impacts*, 2023, **25**, 288

Molecular speciation controls arsenic and lead bioaccessibility in fugitive dusts from sulfidic mine tailings†

Robert A. Root *[a] and Jon Chorover [ab]

Communities nearby mine wastes in arid and semi-arid regions are potentially exposed to high concentrations of toxic metal(loid)s from fugitive dusts deriving from impoundments. To assess the relation between potentially lofted particles and human health risk, we studied the relationship between pharmacokinetic bioaccessibility and metal(loid) molecular speciation for mine tailings dust particulate matter (PM), with elevated levels of arsenic and lead (up to 59 and 34 mmol kg^{-1}, respectively), by coupling *in vitro* bioassay (IVBA) with X-ray absorption spectroscopy (XAS). Mine tailing efflorescent salts (PM_{ES}) and PM from the surface crust (0–1 cm, PM_{SC}) and near surface (0–25 cm) were isolated to <10 μm and <150 μm effective spherical diameter (PM_{10} and PM_{150}) and reacted with synthetic gastric and lung fluid for 30 s to 100 h to investigate toxic metal(loid) release kinetics. Bioaccessible (BAc) fractions of arsenic and lead were about 10 and 100 times greater in gastric than in lung fluid simulant, respectively, and 10–100% of the maximum gastric BAc from PM_{10} and PM_{150} occurred within 30 s, with parabolic dissolution of fine, highly-reactive particles followed by slower release from less soluble sources. Evaporite salts were almost completely solubilized in gastric-fluid simulants. Arsenate within jarosite and sorbed to ferrihydrite, and lead from anglesite, were identified by XAS as the principal contaminant sources in the near surface tailings. In the synthetic lung fluid, arsenic was released continuously to 100 h, suggesting that residence time *in vivo* must be considered for risk determination. Analysis of pre- and post-IVBA PM indicated the release of arsenic in lung fluid was principally from arsenic-substituted jarosite, whereas in synthetic gastric fluid arsenic complexed on ferrihydrite surfaces was preferentially released and subsequently repartitioned to jarosite-like coordination at extended exposures. Lead dissolved at 30 s was subsequently repartitioned back to the solid phase as pyromorphite in phosphate rich lung fluid. The bioaccessibility of lead in surface tailings PM was limited due to robust sequestration in plumbojarosite. Kinetic release of toxic elements in both synthetic biofluids indicated that a single IVBA interval may not adequately describe release dynamics.

Received 27th April 2022
Accepted 7th September 2022

DOI: 10.1039/d2em00182a

rsc.li/espi

Environmental significance

Human health risks from particulate matter (PM) are becoming increasingly clear. Mine tailings serve as PM sources, especially in dry climates. The US Agency for Toxic Substances and Disease Registry shows the top 2 substances of concern are arsenic (#1) and lead (#2), metal(loid)s commonly found in mine tailings. With the associated likelihood of off-site dust transport, inhalation and ingestion of PM can lead to toxic exposures with biological effects controlled by the rate of dissolution *in vivo*. However, the bioavailability, toxicity, and uptake of metal(loid)s also depends on their solid phase speciation, which can be probed with X-ray spectroscopy. This study uniquely combines pharmacokinetic bioassay and solid phase speciation to determine toxic metal(loid) source and kinetic release *in vitro*.

1 Introduction

Mine tailings are a significant source of fugitive dust pollution in the form of atmospheric particulate matter (PM). Since fine-grained, unconsolidated, metalliferous particles can be subjected to suspension and transport by wind (and water), potentially resulting in direct human exposure to toxicants, there is a need to know the lability and precise molecular form or speciation of metal(loid)s that may emit from a tailings

[a]*Department of Environmental Science, University of Arizona, Tucson AZ, USA. E-mail: rroot@arizona.edu; Fax: +1520-626-6782; Tel: +1520-626-1709*

[b]*Arizona Laboratory for Emerging Contaminants, University of Arizona, Tucson AZ, USA*

† Electronic supplementary information (ESI) available: The study site, biofluid simulant formulations, details of synchrotron X-ray analysis; XANES fits; XRD; fit spectra for sulfur, iron, arsenic, and lead; tabulated EXAFS fits; zinc IVBA for PM_{ES} and PM_{SC}, SEM-EDS for PM_{ES}, PM_{10} and PM_{150}, and total elemental analysis of PM_{10} and bulk tailings. See https://doi.org/10.1039/d2em00182a

 This journal is © The Royal Society of Chemistry 2023

Open Access Article. Published on 03 ottobre 2022. Downloaded on 15/09/2024 20:54:19.
This article is licensed under a Creative Commons Attribution 3.0 Unported Licence.

weathering environment.[1] Previous studies point to aeolian transport of fugitive dusts as a primary dispersal mechanism for tailings particles.[2] As such, there is a human health risk of exposure from ingestion and inhalation of fugitive aerosols from mine tailings.[3–5] However, the chemistry and bioavailability of arsenic and lead in dusts from mine wastes are less studied,[6–9] particularly for wastes undergoing diagenetic alteration in (semi)-arid environments.[10–15] Because tailing impoundments often remain barren for decades to centuries due to conditions inhospitable to plant and microbial growth, they are particularly susceptible to erosive forces of wind and rain.[16,17] Exposure to airborne geodusts is expected to increase as climate change intensifies the aridity of drylands.[18] Direct human exposure to PM results in toxic exposures with biological effects that are controlled by the pharmacokinetic rates of PM dissolution in biofluids.[2,19,20]

Primary routes of exposure to geo-dust toxicants include ingestion, inhalation, and dermal absorption. Whereas dermal absorption has been shown to be insignificant for arsenic and lead exposure in humans, fine particles adhered to the skin may be ingested by hand-to-mouth activities, which can be especially problematic for children in proximity to mine tailings.[21] Inhalable and ingestible particles, generally <150 μm effective spherical diameter (ESD), can enter the mouth and nose, whereas particles < 10 μm ESD can pass into the lung. Larger particles that do not pass into the lung (>10 μm ESD) are trapped by cilia as part of the body's filtration defense and are subsequently swallowed.[22] This defensive mechanism protects against inert dust particles that are ingested and excreted, but soluble toxic particles pose an exposure risk.[4] Therefore, both gastric and lung biofluids are relevant considerations for inhalable PM.

Airborne dusts are of particular concern because they are well-known to be associated with widespread lung diseases such as pneumoconiosis (black lung and silicosis) and coccidioidomycosis (Valley Fever). When arsenic and lead are present in tailings-derived dust, toxicity effects present significant human health risk even at low mass concentrations.[23] Exposure to arsenic has negative effects on nearly all body systems, acting as a multi-organ carcinogen, and it has been linked to type-2 diabetes.[24–27] Whereas lead exposure results in toxic poisoning, especially at higher levels of inhalation and ingestion exposure,[28] the principal concern with lead is systemic pediatric neurotoxicity,[29] because studies have shown that young children, with greater cell development compared to adults, experience greater deleterious health impacts to environmental exposures.[30]

Assessment of risk to health from ingested or inhaled contaminants must account for the total toxicant concentration (C_i) and its bioactivity ($a_{i\text{-bio}}$), the fraction absorbed at a target organ.[31] Animal model *in vivo* assays have been used to monitor contaminant uptake and elimination to access relative bioavailability (RBa), and *in vitro* bioassays (IVBA) have been used to determine solubilization of particles under lab-controlled biomimicry to access bioaccessibility (BAc), conditionally-defined as the concentration of an analyte of interest (*e.g.*, As, Pb) released to solution in biofluid simulants.[32,33] Necessarily, total $C_i \geq$ BAc $\geq$ RBa $\geq a_{ibio}$, making BAc a conservative proxy for $a_{i\text{-bio}}$. Whereas prior studies have used IVBA methods to assess arsenic[34,35] and lead[20,36] release from mine tailings, there are few studies that have employed concurrent molecular speciation analysis to test for relations of BAc and local coordination environment of contaminants.[37–39]

We hypothesized that arsenic and lead BAc values would be correlated with their molecular speciation for a range of samples derived from a mine tailings Superfund Site. Therefore, in the present work, arsenic and lead containing sulfide-ore tailings, which had undergone pedogenic weathering in a semi-arid climate, were subjected to IVBA and the time-course of reaction was interrogated by molecular spectroscopy to determine molecular controls over BAc of metalliferous wastes.[15,40] Specifically, we combined macroscopic studies of particle dissolution kinetics in synthetic lung and gastric biofluids with synchrotron X-ray absorption spectroscopy (XAS) of contaminant arsenic and lead, and mineral host sulfur and iron speciation before, during, and after biofluid exposures. Synchrotron XAS proved to be a powerful tool for determining molecular controls over rates of arsenic and lead release to biofluids. The concurrent assessment of BAc and its molecular-level controls can improve risk assessments and inform approaches to remediation action.

2 Materials and methods

2.1 Sampling and characterization

Particulate samples, designated as geo-dust toxic metal sources, were isolated from the surface of tailings impoundments at the Iron King Mine Humboldt Smelter Superfund Site in Dewey-Humboldt, Arizona (see Fig. S1†). Four sample types were collected: (i) PM < 10 μm ESD (PM_{10}) and (ii) PM < 150 μm ESD (PM_{150}), both from the bulk surface (0–25 cm depth) tailings; (iii) surface crust (PM_{SC}) collected at the air-tailings interface from the top 0–1 cm (sieved to < 150 μm ESD); and (iv) efflorescent salts (PM_{ES}), representing those particles that precipitate as ponded mine waters evaporate, collected from dehydration of irrigated tailings used in a greenhouse experiment.[41] These fine-grained particles represent those emitting as fugitive dust from tailings that could be ingested or inhaled.[2,4,23,42,43] Each fraction was air dried at RT and sieved to obtain PM_{150}. Isolation of the PM_{10} was performed *via* cyclone separation, which allows collection of sufficient mass for replicated IVBA reactors without any mechanical crushing, for details see.[44,45]

Total elemental concentrations were analyzed by inductively coupled plasma mass spectrometry (ICP-MS, PerkinElmer, Elan DRC-II) following microwave assisted dissolution by aqua regia (Arizona Laboratory for Emerging Contaminants, ALEC, University of Arizona) and HF, HNO_3, $HClO_4$, and HCl (Activation Labs, Ontario CA). All chemicals were reagent grade or better and all labware was acid washed and metal-free. Total arsenic was analyzed by instrumental neutron activation analysis (INAA) and total iron was analyzed by ICP-AES following dissolution of the tailings in a lithium metaborate flux-fusion (with $LiBO_2$ and $Li_2B_4O_7$) (Activation Labs, Ontario CA).

Open Access Article. Published on 03 ottobre 2022. Downloaded on 15/09/2024 20:54:19. This article is licensed under a Creative Commons Attribution 3.0 Unported Licence.

Certified reference materials were digested and analyzed along with the tailing samples with an acceptance range of ± 10% of the certified value to verify precision and accuracy in sample preparation and analysis. Specific surface area (SSA) was measured by multipoint BET (Brunauer, Emmett, and Teller, Micromeritics Gemini VII 2390 t, Norcross, GA).

2.2 Bioaccessibility of metal(loid)s

BAc was used to assess the metal(loid) exposure risk by monitoring the concentration of As, Pb, and host mineral Fe solubilized into IVBA synthetic biofluid and available for biologic absorption.[8,45,46]

$$\mathrm{BAc}_{(c_i)} = \frac{[c_i]_{\mathrm{IVBA}}}{[c_i]_{\mathrm{total}}} \times 100 \quad (1)$$

where the BAc fraction of element c_i is the concentration dissolved (mmol kg^{-1}) in synthetic lung fluid (SLF) or synthetic gastric fluid (SGF) $[(c_i)_{\mathrm{IVBA}}]$ normalized to the total solid phase concentration $[(c_i)_{\mathrm{total}}]$ in the tailings PM sample.

The lung fluid simulant was a modified Gamble's solution, used previously to mimic the fluid released by Type II alveolar cells and estimate the potential *in vivo* dissolution of metal(-loids) following inhalation of dusts.[47–49] The solution contained a mixture of mineral salts, humectants, and an emulsifier, but omitted proteins to eschew putrefaction (Table S1†), and has been found to be analogous to human alveolar fluid in terms of major components.[50,51] This SLF recipe has been used to determine the BAc of various respirable soil particles including, silica,[52] cadmium,[53] uranium,[54] and lead.[55]

It has been established that among the many *in vitro* gastric extractions, a robust predictor of *in vivo* bioavailability, *i.e.*, a consistently good correlation between *in vitro* BAc and *in vivo* RBa with juvenile swine model for gastric exposures, is a low pH (1.5) fluid buffered with hydrochloric acid and glycine.[56,57] Whereas the large swine body size is favorable for repeated blood sampling, this requires surgery, and swine are expensive and difficult to handle in a laboratory setting.[58] For comparing *in vitro* and *in vivo* bioassays, mouse models are favorable due to their smaller size, lower expense, availability, relative ease of use and are already widely applied in medical research.[1,59–62] However, mouse arsenic metabolism differs from that of humans and their small body weight and blood volume is prohibitive for repeat blood sampling.[63,64] Despite these complications, mice and swine are both considered suitable animal bioassays for validation of *in vitro* bioavailability studies. The chosen IVBA method in this study is representative of both USEPA Method 1340 and the Solubility Bioaccessibility Research Consortium (SRC) assay.[39,65] This SGF mimics conditions of a fasting stomach and was adopted by USEPA bioavailability protocol.[66,67] The SGF, prepared in N_2 sparged deionized water (Milli-Q, 18.2 MΩ) adjusted to pH 1.5 with concentrated HCl (ACS grade) and buffered with 0.4 M glycine, has been established to be appropriate for mining wastes[68] and mine impacted soils, and has been validated as a good predictor of arsenic RBa in contaminated soil.[1,57] This single-step gastric fluid approach was used in the current study.[66,69–71]

Kinetic IVBA experiments with SLF and SGF were carried out in triplicate in batch-mode. In each IVBA vessel, a 0.15 g aliquot of tailings PM was reacted with 15.0 g of SLF or SGF in a metal-free polypropylene tube (VWR, PN 89049-172). The IVBA solution was pre-heated to 37.0 °C to simulate internal body temperature and added to the tailings. The vessel was wrapped with aluminum foil to eschew photoreaction, placed on an end over end rotator in a 37.0 °C incubator at 60 rpm for prescribed durations. Reaction times <5 min were agitated by hand in pre-heated (37.0 °C) biofluid. At each interval, samples were removed from the rotator, centrifuged at 23 600 g, and the supernatant solution was aspirated and syringe filtered to 0.45 μm with acid washed hydrophobic polypropylene GHP membranes (acro-disc, Pall Corp. PN 28139). The filtered supernatant was analyzed for pH to assure changes were <0.5 and by ICP-MS for the elemental BAc concentrations. The concentration of the target analyte that migrated from the solid to aqueous phase was operationally defined as the kinetic-step BAc concentration. The residue was washed with DI water and lyophilized at −45 °C and 0.013 kPa prior to solid phase characterization and spectroscopic analysis. Kinetic studies of the tailing samples included five sample times for the PM_{ES} and PM_{SC} from 0.5 h to 48 h, and nine steps from 30 s to 100 h for the PM_{10} and PM_{150} tailings. Exposure durations were selected to develop (i) relevant particle resident times in lung (days) and gastric (hours) systems and (ii) an understanding of the kinetic release rates of metal(loid)s in these systems at shorter and longer retention times.

2.3 X-ray techniques

Bulk PM minerals were identified on pre- and post-IVBA reacted tailings using synchrotron transmission X-ray diffraction (ST-XRD) at 0.965 Å with a CCD detector for collection of Laue images at beamline 11–3 at the Stanford Synchrotron Radiation Lightsource (SSRL, Menlo Park, CA). Diffractograms were converted to conventional Cu Kα wavelength and normalized to the hkl_{112} quartz reflection (1.818 Å) for comparative analysis. Synchrotron X-ray absorption near-edge spectroscopy (XANES) and extended X-ray absorption fine structure (EXAFS) spectra were collected for speciation of arsenic, iron, (K-edge, 11 867 and 7112 eV) and lead (L_{III}-edge 13 035 eV) at beamline 11–2 at SSRL. Sulfur (K-edge 2472.04 eV) XANES were collected at beamline 4–3 at SSRL. General procedures for XAS collection and data processing were described previously.[15] The mixed ferric phases in PM were resolved using a non-linear least-squares fit to the Fe EXAFS constrained by a two-mineral model for shell-by-shell fits, simultaneously fitting a jarosite model component and a ferrihydrite model component to the tailing PM samples. Details of sample handling, preparation, data collection and analysis are provided in the (ESI†).

3 Results

3.1 Characterization of particulate matter

Both arsenic and lead in the tailing samples exceed the regional background levels ($[\mathrm{As}]_{\mathrm{bkg}}$ = 0.33 mmol kg^{-1}, $[\mathrm{Pb}]_{\mathrm{bkg}}$ =

Open Access Article. Published on 03 ottobre 2022. Downloaded on 15/09/2024 20:54:19.
This article is licensed under a Creative Commons Attribution 3.0 Unported Licence.

0.10 mmol kg^{-1}),[72] with tailing PM exhibiting multi-metal enrichment.[15] Total metal(loid) concentration increased with decreasing particle-size, consistent with previous studies of mine tailings[8,12] (Table 1). The iron-normalized molar concentrations of arsenic and lead (As : Fe, Pb : Fe) varied by sample type, with values of about 0.02 and 0.01, respectively, for PM_{10} and PM_{SC}, while PM_{150} had lower values of about 0.015 and 0.005, respectively, indicating a relative enrichment in both arsenic and lead in PM_{10}. The PM_{ES}, which had <63 μm ESD, were completely soluble in aqua regia digestion, but had only *ca.* 0.1% of the arsenic and lead content of the other PM. Further, in comparison to the other geodusts, the PM_{ES} were depleted in arsenic and lead with As : Fe and Pb : Fe values of 0.0002 and 0.0026. However, PM_{ES} had almost 10*x* elevated Zn ($[Zn]_{ES}$ = 496 μmol g^{-1}) compared to other PM (*e.g.* $[Zn]_{150}$ = 59, $[Zn]_{SC}$ = 46.5 μmol g^{-1}) (Fig. S2 and S3†). Despite the greater solubility of efflorescent salts, the arsenic and lead inhalation exposures from PM_{ES} were expected to be lower than other the particles as exposure is a function of total concentration and solubility (Table 1).

Table 1 Bioaccessible iron, arsenic, and lead in Iron King Mine Tailings

Sample	[Fe]			[As]		[Pb]	
Total concentration[a] (mmol·kg^{-1})							
PM_{10}	3330			58.7		34.0	
PM_{150}	2220			34.3		11.4	
PM_{SC}	1890			38.3		19.0	
PM_{ES}	93.1			0.0220		0.0222	
SRM 2782	4820			2.22		2.77	
Background[b]	na			0.297		0.101	
Molecular speciation[c]							
	fh	jar	pyt■/cop*	As^{V}-fh	As^{V}-jar	Pb-jar	ang
PM_{10}	55	41	3■	24	76	86	14
PM_{150}	30	61	8■	38	62	71	29
PM_{SC}	39	52	10■	46	54	na	
PM_{ES}	26	39	35*	<DL		<DL	
Maximum percent BAc lung[d]							
PM_{10}	1.55[1]			3.64[2]		0.016[1]	
PM_{150}	0.15[3]			1.31[2]		0.022[2]	
PM_{SC}	0.12[4]			0.37[5]		0.02[5]	
PM_{ES}	28.3[4]			2.3[4]		67.5[6]	
SRM 2782	na			1.1[2]		<0.01	
Percent BAc lung 24 h							
PM_{10}	0.54[a]			1.16[d]		0.003[g]	
PM_{150}	0.07[b]			0.74[e]		0.003[g]	
PM_{SC}	0.07[b]			0.22[f]		0.006[g]	
PM_{ES}	2.3[c]			0.74[e]		7.8[h]	
Maximum percent BAc gastric[d]							
PM_{10}	19.1[7]			11.7[7]		3.00[7]	
PM_{150}	32.9[7]			25.3[7]		18.2[7]	
PM_{SC}	5.8[5]			13.3[5]		0.87[8]	
PM_{ES}	93.3[5]			87.9[5]		86.3[5]	
SRM 2782	na			25.4[7]		92.5[7]	
Percent BAc gastric 1 h							
PM_{10}	2.9[i]			7.8[l]		0.77[o]	
PM_{150}	3.6[i]			9.9[l]		0.66[o]	
PM_{SC}	1.1[j]			4.3[m]		0.11[p]	
PM_{ES}	76.7[k]			44.9[n]		74.5[q]	

[a] Total concentration in PM_{10}, PM_{150}, and PM_{SC} determined by $Li_2B_4O_7$/$LiBO_2$ fusion with ICP-MS detection, PM_{ES} total concentrations determined by aqua regia digest with ICP-MS detection, SRM 2782 is the assigned NIST value. [b] Background is the site-specific level.[73] [c] Molecular speciation of each element as determined by XAS, [a–q] BAc significantly different at $p < 0.05$ for 24 h SLF and 1 h SGF. [d] Maximum BAc at specified time points: [1]30 s, [2]168 h (7d), [3]5 min, [4]0.5 h, [5]48 h, [6]1 h, [7]100 h, [8]24 h; fh = ferrihydrite, jar = jarosite, pyt■ = pyrite (from Hayes *et al.*, 2015), ang = anglesite, cop* = copiapite, <DL = less than detection limit, na = not applicable, IVBA results reported are average of triplicates.

Major crystalline phases in PM_{10}, PM_{150}, and PM_{SC} determined by synchrotron XRD were quartz [SiO_2], albite [$NaAlSi_3O_8$], gypsum [$CaSO_4 \cdot 2H_2O$], pyrite [FeS_2], jarosite [$KFe_3(SO_4)_2(OH)_6$], and chlorite [$(Mg,Fe)_5Al_2Si_3O_{10}(OH)_8$] (Table 1). Crystalline arsenic or lead phases were not detected by XRD (detection limit ~2 wt%). Efflorescent salts (PM_{ES}) comprised gypsum, magnesiocopiapite [$MgFe^{(III)}{}_4(SO_4)_6(OH)_2 \cdot 20H_2O$], goslarite [$ZnSO_4 \cdot 7H_2O$], copiapite [$Fe^{(II)}Fe^{(III)}{}_4(SO_4)_6(OH)_2 \ldots 20H_2O$], hydrated ferric sulfate salts [$Fe_2(SO_4)_3 \cdot xH_2O$], ferrihydrite [$Fe_2O_3 \cdot 5H_2O$], and jarosite. The effective enrichment of metal(loid)s in the finest particulates was due to depletion of coarser primary silicate minerals in the fine size fractions.

3.2 Lung fluid IVBA is

3.2.1 Kinetics. The fractional releases of arsenic and lead, and the dissolution of host ferric minerals were interrogated with a circumneutral SLF to assess *in vitro* kinetic exposure representing inhalation of PM, where elemental release to the biofluid simulant represented the BAc fraction relative to the total PM concentration. Synthetic lung fluid IVBA showed generally low BAc for metal(loid)s in each PM compared to gastric exposures (about 1–10%) (Table 1), with the greatest relative release occurring at the shortest time-points (*e.g.*, minutes) (Fig. 1). Following this rapid pharmacokinetic release, in the closed IVBA batch reaction, iron and lead were observed to repartition back to the solid phase at longer exposures (>24 h). Arsenic showed release to SLF from PM_{10}, PM_{150} and PM_{SC}, increasing at extended times, whereas PM_{ES} at 48 h showed no significant difference from the maximum release at 5 min. The BET SSA for PM_{150} increased from 2.3 m^2 g^{-1} (unreacted) to 9.6 m^2 g^{-1} after 48 h SLF as higher specific surface area particles or mineral coatings precipitated in the lung fluid.

The PM_{10}, which showed approximately 2*x* enrichment of arsenic and lead relative to the PM_{150} and PM_{SC} and over 2000*x* enrichment relative to PM_{ES}, had a maximum arsenic BAc of 3.6% compared to 2.2% for PM_{150}, 0.37% in PM_{SC}, and 2.3% in PM_{ES} (Table 1). Lead BAc was not significantly different ($p > 0.05$) for PM_{10}, PM_{150}, and PM_{SC} at 0.02%, but 67.5% in PM_{ES}.

At 24 h in SLF, the generally used IVBA time point for lung exposure, the arsenic released from the PM_{10} was more than 2*x* PM_{150}, and the BAc was significantly larger ($p < 0.05$) than each of the other PM. The lead BAc was low and not significantly different among PM_{10}, PM_{150} and PM_{SC}; the release at 24 h from PM_{ES} was the highest BAc (7.8%), and was three orders-of-

Open Access Article. Published on 03 ottobre 2022. Downloaded on 15/09/2024 20:54:19.
This article is licensed under a Creative Commons Attribution 3.0 Unported Licence.

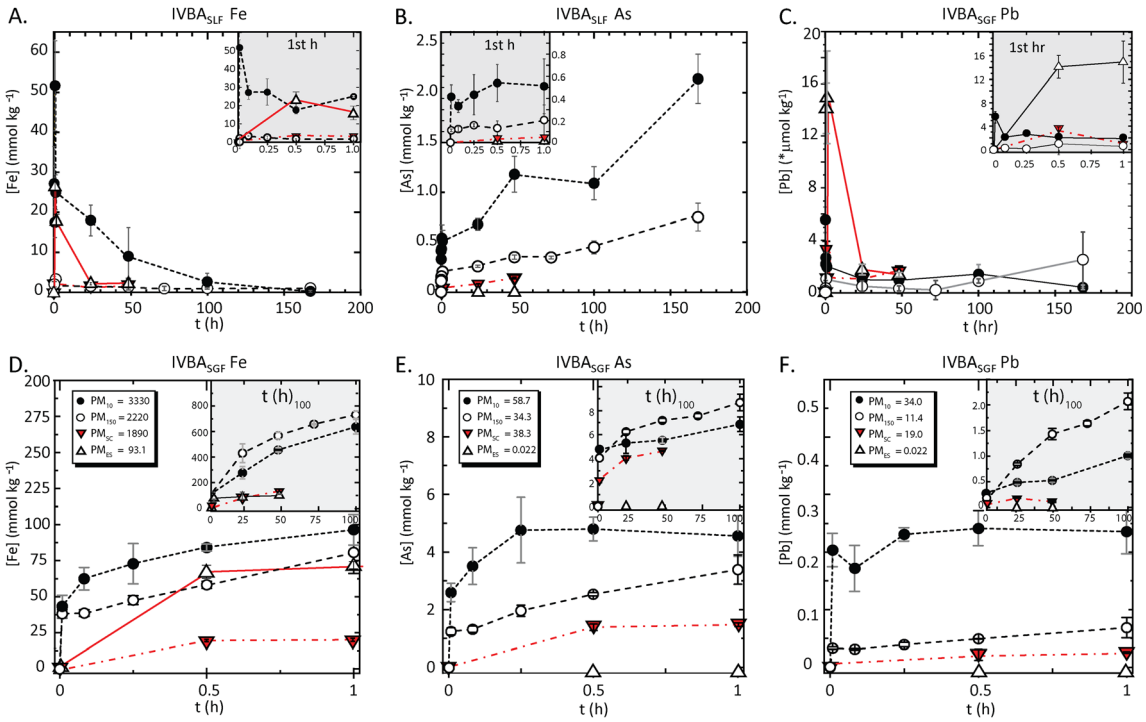

Fig. 1 Kinetic bioaccessibility of iron, arsenic, and lead from particulate matter (PM) in synthetic lung and gastric fluids (SLF, SGF). Data shows moles released to solution per unit mass of solid PM (mmol kg^{-1}, *Pb SLF is µmol kg^{-1}) for iron (left), arsenic (center) and lead (right) from PM_{10} (solid circle), PM_{150} (open circle), PM_{SC} (downward triangle), PM_{ES} (open triangle), in synthetic lung (A–C) fluid to 168 h and gastric (D–F) fluid to 1 h. Inset box details the <1 h interval for SLF and >1 h for SGF. Initial PM concentrations (mmol kg^{-1}) are shown above and given in Table 1.

magnitude greater than the other PM. For lead and iron, the maximum release was at the shortest time points (<1 h). Whereas the arsenic and lead mass concentrations (mg kg^{-1}, ppm) in individual PM particles were nearly equal, the mole fraction release of arsenic to SLF was about 150*x* higher than that of lead in PM_{10} and PM_{150} and 20*x* PM_{SC}; while PM_{ES} showed lead BAc almost 30x greater than arsenic.

3.2.2 Speciation. Micrographs of unreacted PM_{ES} by SEM showed particles with an effective spherical diameter of less than 50 µm and abundant large (25–50 µm) elongated prismatic columns of gypsum; post bioassay imaging was not possible as soluble salts were mostly dissolved *in vitro* (Fig. S4†). Morphological changes were observed by SEM-EDS in the unreacted compared to SLF-reacted PM_{10} and PM_{150} (Fig. 3, S4 and S5†), which showed electron-transparent (*i.e.*, relatively low density) 4–5 µm long acicular neo-precipitates (Fig. S6†). Comparing normalized (to quartz hkl_{112}) X-ray diffractograms (Cu Kα) of 48 h SLF-reacted PM_{150} to the unreacted PM_{150} showed a new broad feature centered at 20° 2θ (4.13 Å) and a new sharp reflection at 13.5° 2θ (6.4 Å)(Fig. S7†). The broad feature was attributed to newly formed hydrous ferric oxide (HFO) or ferrihydrite ($PM_{150}\log\Omega_{24h}$ = 4.4; calculated from the aqueous chemistry of PM_{150} at 24 h in SLF), while the sharp reflection at ~6.4 Å was a fair fit (with multiple overlapping peaks) to the calcium sulfate hemihydrate mineral bassanite ($CaSO_4\cdot\frac{1}{2}H_2O$), consistent with the micrograph images of acicular or columnar crystals (Fig. S6†). Pyromorphite, an expected sink for lead in high phosphate environments, with a maximum reflection at 30.5° 2θ (100% hkl_{112} = 2.92 Å), was obscured by an overlapped jarosite peak at 30.14° 2θ (10% hkl_{202} = 2.97 Å) in PM_{10} and PM_{150} (Fig. S7 and S8†). Mineralogical changes in PM_{10} were less apparent in XRD diffractograms, except increased relative intensity of peaks from gypsum post SLF IVBA.

3.2.2.1 Iron species. Evaluation of the PM_{10} Fe Kα XANES pre-edge (7110–7118 eV), a feature resulting from an allowed transition of the 1s electron to a 3d orbital, showed slight changes in the three assigned peaks (*a-c*) that make up the pre-edge (Fig. 2A). The lowest energy peak (*a*) at 7112 eV was present in jarosite and absent in ferrihydrite. The *a* peak decreased in the 48 h SLF reacted sample compared to the unreacted PM_{10} particles. Additionally, the subsequent pre-edge peaks (*b*) at 7113 eV and (*c*) at 7115 eV show a relative increase in *c*, over *b*, post IVBA. The pre-edge in the PM_{150} showed slight changes in the three assigned peaks (*a–c*), similar to PM_{10} with the (*a*) peak diminished in SLF at 48 h (Fig. S9†). Linear combination fits (LCF) to the PM_{10} Fe EXAFS showed that the iron in the unreacted tailings was comprised of jarosite (41%), ferrihydrite (55%) and pyrite (3%), PM_{150} was jarosite (61%), ferrihydrite (30%) and pyrite (8%), PM_{SC} had, jarosite (52%), ferrihydrite (39%), and pyrite (10%), and unreacted PM_{ES} was jarosite (39%), ferrihydrite (26%), and copiapite (35%). Iron EXAFS of unreacted and 48 h post IVBA PM tailings were compared. The 1st shell feature in the Fourier transformed Fe Kα EXAFS, attributed to the Fe^{III}–O_6 backscattering, increased in amplitude for the 48 h SLF-reacted PM_{10} relative to the unreacted PM_{10} and the Fe–O radial distance increased from 1.94 Å to 1.97

Open Access Article. Published on 03 ottobre 2022. Downloaded on 15/09/2024 20:54:19.
This article is licensed under a Creative Commons Attribution 3.0 Unported Licence.

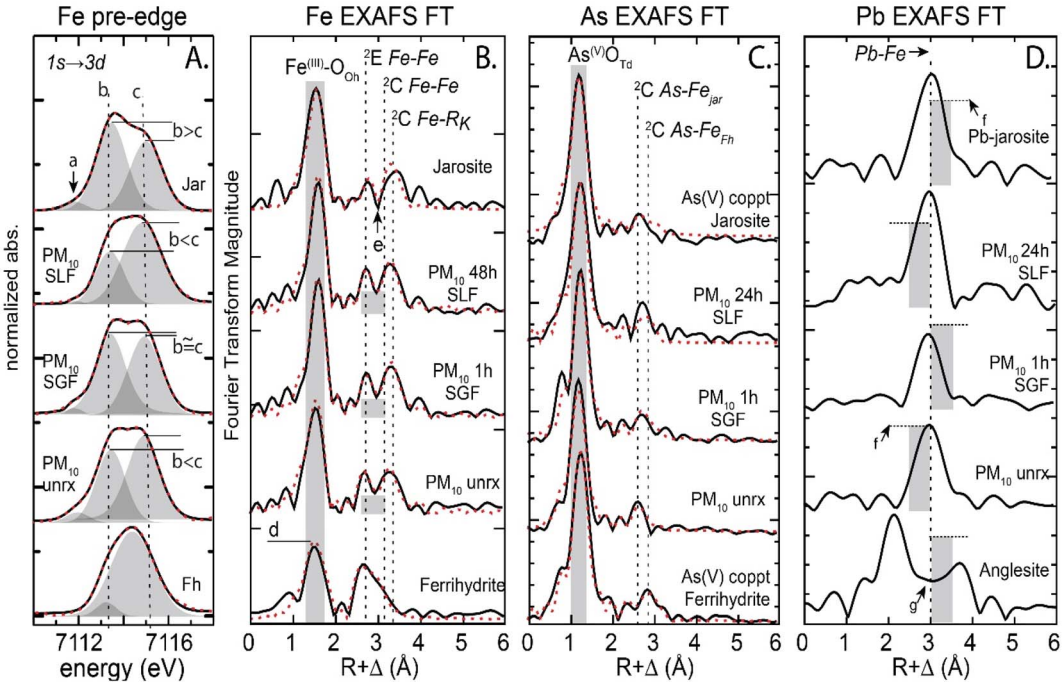

Fig. 2 Iron XANES pre-edge and iron, arsenic, and lead EXAFS Fourier transform of unreacted and IVBA reacted PM_{10} from Iron King mine tailings. Panel A shows Fe XANES pre-edge, with peaks [a–c] characteristic of ferrihydrite v jarosite in oxidized sulfidic tailings. Panel B shows the EXAFS FT for PM_{10} reacted in lung and gastric fluid *in vitro*, [d]indicates Fe–O backscattering and highlights FWHM peak change for ferrihydrite v jarosite and [e]indicates separation of edge sharing Fe–S/Fe and corner sharing Fe–Fe in ferrihydrite and jarosite, fits shown in Table S2.† Panel C shows As EXFAS FT with first shell As–O at 1.68 ± 0.02 Å and second shell As–Fe Δ0.02 Å. Panel D shows Pb EXFAS FT, [f]Pb–Fe FT peak amplitude is greater for PM_{10} unrx. [g]indicates region of FT where Pb–O features would be observed for Pb-sorbed ferrihydrite.

Å (Fig. 2B and S10,Table S2†). Second shell contributions for near neighbor iron backscattering atoms varied with the contribution of jarosite and ferrihydrite, and fits were constrained with a binary structural model for fitting. Backscatterer Fe–Fe distances varied by the major contribution from the identified species, where longer corner sharing Fe–Fe distances at 3.64 ± 0.01 Å and Fe–S at 3.24 ± 0.01 Å were assigned to jarosite and shorter Fe–Fe distances of 3.07 ± 0.02 Å and 3.36 ± 0.01 Å were assigned to ferrihydrite. At 1 h, PM_{10} showed a decrease by about 50% in coordination of the Fe–Fe at 3.08 ± 0.1 Å and 3.35 ± 0.1 Å from 1.5 and 3.1 to 0.7 and 1.4, respectively (Table S2†). These distances were attributed to the contribution from Fe–Fe backscattering from edge-sharing (^{2}E) and corner-sharing (^{2}C) Fe^{III} octahedra in ferrihydrite, respectively.[74] The Fe second shell contribution showed a decrease in the contribution from ferrihydrite at 1 h and longer, *e.g.*,48 h (Table S2†). No significant changes were observed in the jarosite associated backscattering near neighbors. The post SLF IVBA PM_{150} Fe EXAFS showed small decreases in coordination of the Fe–S and Fe–Fe to 1.4 and 1.2, respectively (Fig. S11 and Table S3†). While the minor change noted in the jarosite associated Fe–Fe backscattering near neighbors at 3.63 Å was within the error of fitting coordination numbers in complex matrices, it is nonetheless consistent with a reduction in the jarosite contribution to the EXAFS signal. Fitting the post IVBA PM_{ES} showed significant alteration of the Fe second shell neighbors with a depletion in Fe–S at 3.27 Å and alteration of the Fe–Fe 3.26 Å and 3.40 Å distances associated with ferrihydrite (Table S4†). The complex dissolution and reprecipitation in the PM_{ES} is not resolvable by Fe EXAFS but does indicate a loss of Fe–S second shell ligand, likely attributed to dissolution and loss of soluble ferric sulfate salts and jarosite.

3.2.2.2 Sulfur species. The unreacted PM_{10} sulfur speciation was dominated by gypsum (49.1%), which was depleted by extended incubation *in vitro* (Table S5, Fig S12 and S13†). The relative contribution of pyrite to the sulfur XANES increased with each time step, as sulfate species were solubilized. Other components of the fits increased concomitantly, with the relative contribution of pyrite doubling, and the jarosite signal increasing slightly less than the ferrihydrite-adsorbed sulfate contribution. Sulfur speciation in unreacted PM_{150} was mostly jarosite (60%), and at long reaction times 7 d in the SLF the contribution from pyrite was unchanged, jarosite increased to over 80% of the S signal while gypsum and adsorbed sulfate were depleted relative to other species.

3.2.2.3 Arsenic species. The solid phase arsenic speciation at each kinetic step probed by EXAFS showed $As^{(V)}$–O_4 in tetrahedral coordination at 1.68 ± 0.02 Å (Table S6 and S7†). The As EXAFS showed changes in second shell ligand distances as a function of the mixing ratio of ferrihydrite and jarosite associated arsenate (Fig. S14†). The spectral contribution from jarosite associated arsenate was greater than arsenic sorbed ferrihydrite in PM_{10}, PM_{150}, and PM_{SC} and was not detectable in PM_{ES} (Table 1). In the unreacted PM_{10}, 76% of the arsenic was

Open Access Article. Published on 03 ottobre 2022. Downloaded on 15/09/2024 20:54:19. This article is licensed under a Creative Commons Attribution 3.0 Unported Licence.

associated with jarosite and 24% with ferrihydrite, even though PM_{10} was enriched (with respect to iron) in non-arsenic associated ferrihydrite relative to PM_{150} and PM_{SC} (Table 1). Unreacted PM_{10} had a longer As–Fe distance of 3.32 Å compared to the unreacted PM_{150} and PM_{SC}, which was 3.28 Å (Table S6–S8†). Post SLF IVBA, PM_{10} had a slight lengthening of the As–Fe distance from 3.32 Å to 3.34 Å at 48 h. The small 0.02 Å change (>estimated fitting error ±0.015 Å) supports, but is not compelling evidence for, a greater contribution to the EXAFS signal from arsenate complexes with slightly longer As–Fe distances at 48 h and an attendant reduction in the signal from shorter As–Fe bonds (<3.30 Å). The PM_{150} As EXAFS showed a lengthening of the As–Fe second shell ligand at 48 h to 3.32 Å, compared to the unreacted PM_{150} at 3.28 Å.

3.2.2.4 Lead species. The unreacted PM_{10} and PM_{150} lead speciation was best described by two species, plumbojarosite and anglesite. The PM_{10} particles were enriched (86%) in plumbojarosite relative to PM_{150} (71%) (Table 1). Reaction in SLF showed no significant change in lead speciation for PM_{10}, while PM_{150} showed a decrease in plumbojarosite and consequent increase in anglesite over 7d *in vitro* (Table S9 and Fig S15†).

3.3 Gastric fluid IVBA

Exposure risk from ingestion of metal(loid)s from IK tailings was interrogated with acidified 0.4 M glycine at pH 1.5 as a gastric fluid surrogate. The ≤1 h exposures of PM to SGF represents biorelevant durations of residence times expected in the GI track and may better represent *in vivo* exposures compared to long incubations[46] (Fig. 1 and Table 1). However, while the long duration SGF assays (>1 h) may not represent realistic *in vivo* residence times, these nonetheless indicated mechanisms of dissolution and reprecipitation that could occur with extended bioassay or physiological mechanisms not mimicked *in vitro*. Synthetic gastric IVBA showed generally higher BAc for each element in each PM relative to synthetic lung fluid IVBA.

3.3.1 Kinetics. The metal(loid) release rate to synthetic gastric fluid from each PM was greatest at the early intervals. For example, a parabolic release curve was observed with arsenic reaching 8.2% and 9.9% after just 0.25 h for PM_{10} and PM_{150}, respectively (Fig. 1). The release of total metal(loid)s from PM_{10} was greater than other PM for time steps ≤ 1 h, but at 100 h PM_{150} had the greatest release. After the first hour, the asymptotic release of arsenic approached a BAc of 10% PM_{10}, 25% for PM_{150}, 13% for PM_{SC}, and nearly 90% for PM_{ES} (Fig. 1 and Table 1). The iron and arsenic released from PM_{SC} showed an increase at each successive step to 48 h where 5.8% and 13.3% of the total iron and arsenic, respectively was dissolved, a trend similar to the PM_{10} and PM_{150}. Lead released from PM_{SC} had a maximum at 24 h and a return to the solid phase at 48 h. Release kinetics from PM_{ES} showed a relative increase at each successive interval to termination at 48 h, where 93.2%, 87.9%, and 86.3% of the iron, arsenic and lead were released, respectively. The BET SSA for PM_{150} decreased from 2.3 $m^2\ g^{-1}$ (unreacted) to 1.6 $m^2\ g^{-1}$ after 1 h in SGF (and 1.1 $m^2\ g^{-1}$ after 48 h), indicating dissolution of higher surface area particles in the acidic fluid.

3.3.2 Speciation. Relative to the unreacted PM, the post SGF IVBA XRD diffractograms showed a relative decrease in the jarosite signal and nearly unchanged pyrite peaks, and a flattening of the lower 2θ baseline attributed to loss of amorphous and short-range order ferric hydroxides or ferrihydrite (Fig. S7 and S8†). Morphological changes were observed in SEM micrographs of the unreacted PM_{150} tailings compared to 1 h in SGF (Fig. 3). At 1 h in SGF, rough surface texture is reduced, and at extended times (48 h) grains have lost the fine texture (Fig. 3 A–C).

3.3.2.1 Iron species. Linear combination fits (LCF) to the Fe EXAFS for unreacted tailings are given (Table 1). Shell by shell fitting showed PM_{10} reaction in SGF for 1 h resulted in about 50% diminished contribution of ferrihydrite as shown in the Fe–Fe distances at 3.08 Å and 3.35 Å, and this effect increased at extended reaction times (Table S2†). Additionally, the Fe EXAFS FT showed an amplitude increase and narrowing of the Fe–O in the first shell peak after 1 h reaction in SGF (Fig. 2). There was no significant change in PM_{150} at 3.08 Å but a 25% diminished contribution and 0.04 Å reduction in distance from 3.38 Å to 3.34 Å in the longer Fe–Fe after 1 h reaction in SGF (Table S3†). The changes noted in the ferrihydrite associated Fe–Fe backscattering near neighbors at approximately 3.04 Å and 3.34 Å were consistent with a reduction in the ferrihydrite to the EXAFS signal for PM_{10} and PM_{150}. The jarosite contribution to the EXAFS spectra from PM_{10} showed no significant change in the coordination number or radial distance of the Fe backscatters after 1 h in SGF (Table S2†). At 48 h, the PM_{10} jarosite contribution showed a reduction in coordination of the Fe–Fe corner sharing octahedra at 3.63 Å of about 3.2 to 2.0 and 1.6 to 1.0 for Fe–S at 3.27 Å. Insufficient PM_{ES} remained for XAS after IVBA in SGF.

3.3.2.2 Sulfur species. Similar to SLF, reaction in the acidic SGF showed the PM_{10} and PM_{150} contribution from gypsum to the sulfur XANES spectra decreased at each interval *in vitro* (Table S5 and Fig S12†), and the contribution of pyrite to the sulfur XANES increased relative to the unreacted PM as the sulfate species were solubilized (Fig. S13†). At the longest incubation *in vitro*, the sulfur XANES signal was dominated by jarosite in PM_{10} and PM_{150}, as other species dissolved.

3.3.2.3 Arsenic species. The arsenic speciation, determined to be arsenate, did not change during SGF (or SLF) IVBA (Table S6 and S7†). Second shell As–Fe backscattering at 3.28 Å in PM_{150} increased slightly in coordination number from 1.5 to 2.2 at 1 h. The second shell As–Fe distance in PM_{10} shortened post 1 h SGF, from 3.32 Å to 3.30 Å at 1 h and 3.29 Å at 24 h, indicating preferential removal of longer range As–Fe. The As EXAFS also showed changes in second shell ligand distances of As–Fe as a function of the mixing ratio of ferrihydrite and jarosite associated arsenate.

3.3.2.4 Lead species. Analysis of Pb-L_{III} EXAFS indicated that PM_{10} contained lead mostly in plumbojarosite, with good alignment of backscattering oscillations in k space ($Å^{-1}$) but a reduced amplitude in the $\chi(k)\cdot k^3$ EXAFS compared to reference plumbojarosite (Fig. S15†). The amplitude reduction was

Open Access Article. Published on 03 ottobre 2022. Downloaded on 15/09/2024 20:54:19.
This article is licensed under a Creative Commons Attribution 3.0 Unported Licence.

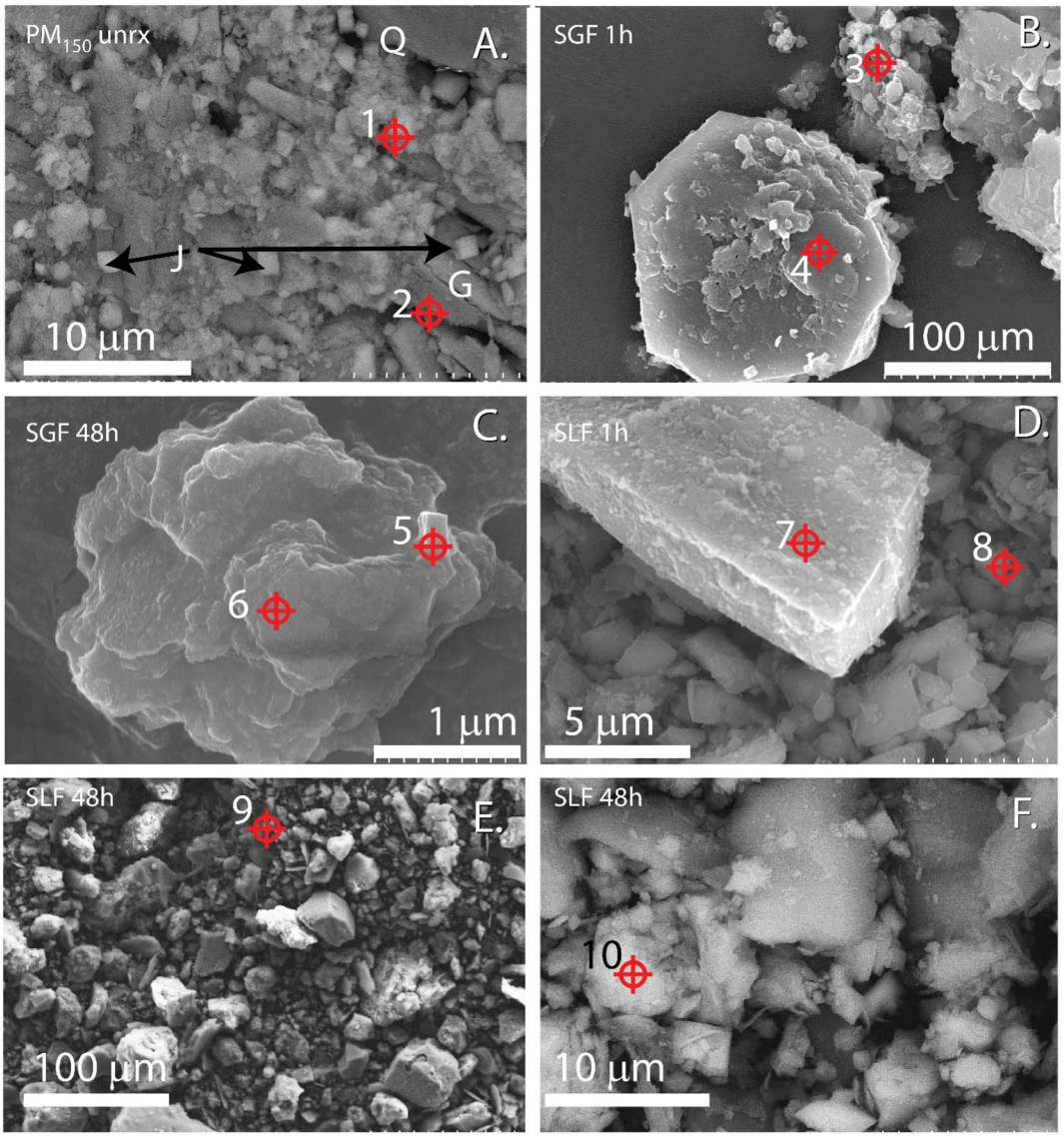

Fig. 3 Electron micrographs of <150 µm effective spherical diameter particulate matter (PM_{150}) isolated from IKMHSS tailings unreacted (A) and after *in vitro* gastric simulant bioassay for 1 hour (B), and 48 hours (C), and lung fluid for 1 h (D) and 48 h (E and F). Crosshairs indicate EDS spots,[1–10] spectra given in Fig. S5.† Panel (A) J = jarosite, Q = quartz, G = gypsum. Scale bar indicates magnification.

attributed to out of phase lead -bearing solids *e.g.* anglesite, consistent with previously reported tailings materials.[20] Reaction in SGF showed a decrease in the contribution of plumbojarosite for PM_{10} and PM_{150} after 1 h. (Table S9†).

4 Discussion

Fugitive dusts in arid and semi-arid environments exhibit hygroscopic growth *in vivo* under conditions of high humidity that enhance alveolar deposition and inhibit lung clearance.[76] When particles finer than 10 µm effective spherical diameter (PM_{10}) pass the tracheobronchial system into the lungs, the relative solubilities of the remaining compounds will dictate what dissolves into extracellular fluids, while insoluble compounds can accumulate as particles in the lungs.[77] Larger particles (>PM_{10}) that do not pass into the respiratory regions of the lung are trapped in mucus by cilia as part of the body's filtration defense. The muco-ciliary escalator mechanism clears larger particles from the airway toward the pharynx, where they are swallowed and become susceptible to gastric fluid dissolution.[78]

The maximum mass release of toxins in synthetic lung fluid at ≤24 h (Table 1), and the extrapolated risk to human health from inhalation exposures, from Iron King mine tailings particles for arsenic was $PM_{10} > PM_{150} > PM_{SC} > PM_{ES}$ and for lead was $PM_{ES} > PM_{10} > PM_{SC} > PM_{150}$. The pharmacokinetic release to SLF from PM_{10} shows greatest risk at short duration exposures (<0.5 h) for lead and a delayed exposure risk for arsenic, with the greatest arsenic release measured in this study at the longest time step (Fig. 1). Combining sorbate elemental analysis with sorbent multi-element XAS, XRD, SEM and BET at several bio-relevant kinetic steps indicated arsenic-substituted jarosite

Open Access Article. Published on 03 ottobre 2022. Downloaded on 15/09/2024 20:54:19. This article is licensed under a Creative Commons Attribution 3.0 Unported Licence.

was the most bioaccessible species with respect to arsenic, and the toxic metalloid host phase posing the most risk in lung fluid. Precipitation of arsenic or lead bearing minerals in lung fluid can remove a contaminant from the dissolved phase, but it is unclear the extent to which such *in vivo* lung fluids achieve supersaturation and, if so, neoformed particles may also act as irritants and long-term point-sources of chronic exposure at extended residence times (*e.g.*, years). However, in lung tissue, the larger volume of fluid and continuous throughflux of new fluid interacting per unit mass of particle is likely to preclude, to some degree, the back reaction (*i.e.*, secondary precipitation formation).

4.1 Arsenic speciation

In unreacted PM, arsenic was distributed between ferrihydrite and jarosite (Table 1 and Fig. S14†). The surface crust had the highest ferrihydrite associated arsenic, lowest jarosite associated arsenic, and the lowest 24 h BAc in lung fluid, 0.22% (and lowest maximum 0.37% at 48 h) and lowest in gastric fluid, 4.3% at <1 h. With increased content of short-range ordered minerals like ferrihydrite in metalliferous-mine tailings, arsenic shows a corresponding decrease in bioaccessibility for SGF and SLF, attributable to the high activity of high-affinity sites for surface complexation of arsenate.[45]

The reported EXAFS determined As–Fe interatomic distances in jarosites are: 3.25–3.26 Å for arsenic co-precipitated jarosite;[79–81] 3.35 Å for high arsenic jarosite loadings (17 mole%, possible contribution from scorodite);[75,80,82] and 3.22 Å for ^{2}C coordination of As-adsorbed jarosite.[79] Ferrihydrite with low to moderate arsenic loading (Fe : As > 50) displays As–Fe ^{2}C coordination at 3.28 Å for bidentate arsenate tetrahedra corner-sharing oxygens with two edge linked iron octahedra, as determined by EXAFS and DFT calculations.[74] These distances are shorter than the longer distances of 3.32 Å (^{2}C) reported for colloidal amorphous ferric arsenate.[74,83] Arsenic-rich amorphous particles have been reported to occur as highly-aggregated clusters, 10 to 100 nm in size, composed of corner-linked iron octahedra in bidentate-binuclear complexation with arsenate.[84] While the arsenic in the PM was distributed between surface complexed arsenate on ferrihydrite and substituted for sulfate in jarosite, the long As–Fe distance of 3.30–3.34 Å observed in the unreacted PM_{10} indicated arsenic was also associated with colloidal amorphous ferric arsenate in ^{2}C coordination,[84] whereas the relatively shorter As–Fe distances in PM_{150} of 3.27–3.28 Å are in agreement with bidentate binuclear arsenic adsorbed on ferrihydrite reactive surface sites.[74] The PM_{10} displayed relatively longer As–Fe bonds (>3.30 Å), consistent with high arsenic loading of ferric hydroxide octahedra. Whether high arsenic ferric solids were linked chains[80] or ferric arsenate clusters,[83] is beyond the scope of this study.[74]

4.1.1 SGF. Gastric IVBA carried out to 100 hours approaches an extreme exposure duration. Here, the 1 h and less duration exposures are emphasized as those that are physiologically relevant (Fig. 1). However, long kinetic steps were applied to explore positive and negative interferences in toxin release from competing reactions and dissolution mechanisms *in vitro* that may not mimic *in vivo* physiology. In contrast to SLF, changes in the post SGF atomic coordination of arsenic showed slight shortening of the As–Fe distance from 3.32 Å (PM_{10}) and 3.28 Å (PM_{150}) to 3.28 Å and 3.27 Å, respectively, consistent with a reduction in the contribution of arsenate coprecipitated with ferrihydrite 3.28 Å[74] and an increase in the contribution of the shorter distance As–Fe jarosite component of 3.27 Å.[75,80] Arsenic liberated from surface complexation sites on ferrihydrite was the major contributor to the SGF BAc at initial time points, and at extended incubations *in vitro* arsenic may partition back to the solid phase in As-jarosite or Pb–As-jarosite, or as a surface complex on freshly precipitated β-FeOOH (PM_{150} $\log \Omega_{100h} = 2.43$). Although neo-precipitate ferric hydroxides were observed to be supersaturated in the closed and extended SGF IVBA, they would not be expected to form in the gastrointestinal tract *in vivo* and would therefore not likely serve as a sink for dissolved arsenic in a physiological system. However, under the acid conditions in gastric fluid, arsenic released from soluble phases like calcium arsenate or arseniosiderite could adsorb to co-occurring, sparingly-soluble ferric hydroxides thus attenuating the measured bioaccessible fraction.[85,86] At the acid pH of SGF (1.5), precipitation of ferrihydrite was not thermodynamically favorable (PM_{150} $\log \Omega_{100\ h\text{-}SGF} = -2.2$), although there was a thermodynamic drive for akaganeite and plumbojarosite (PM_{150} $\log \Omega_{100\ h} = 11.3$) precipitation. The pre-existence of jarosite surfaces could serve as a template to decrease the activation energy (degree of supersaturation) required for nucleation and crystal growth,[87,88] which could sequester both arsenate and lead during long term low pH SGF IVBA exposure. Because ingestion exposure to PM_{ES} exhibited rapid solubilization on the time scale of minutes to hours, this suggests that total concentration was a reasonable indicator of BAc of arsenic and lead in efflorescent salts. However, the total arsenic concentration in the PM_{ES} was 3 orders of magnitude lower than the other PM (Table 1). Whereas the 1 h SGF bioaccessible fraction of PM_{10}, PM_{150} and PM_{SC} were all much lower (4.3–9.9%) compared to PM_{ES} (44.9%), the total mass of arsenic released per gram of geodust was much lower in the PM_{ES} ($[As_{ES}]_T = 0.022$ μmol g^{-1}), and therefore PM_{ES} poses a lower IVBA determined risk of arsenic exposure.

4.1.2 SLF. About 20% of the total SLF released arsenic occurred at 30 s and aqueous arsenic concentrations increased in all PM at each kinetic measurement step, releasing about 80% of the BAc arsenic after the initial pulse (Fig. 1). Investigation of SLF arsenic bioaccessibility of PM_{20} from Au mining wastes from southern Australia, where the principal arsenic bearing phase was scorodite ($FeAsO_4 \cdot 2H_2O$), showed a rapid release followed by a modest increase in arsenic dissolution to 24 h, but in that study total BAc arsenic was <0.1%.[89] Here, BAc values were more than an order of magnitude higher, indicating that the mixture of arsenate-rich jarosite and ferrihydrite pose a much greater inhalation risk than scorodite dominated tailings. Additionally, studies have shown soil arsenic BAc varies with speciation; BAc showed jarosite > ferrihydrite > scorodite > arsenopyrite.[90]

Open Access Article. Published on 03 ottobre 2022. Downloaded on 15/09/2024 20:54:19.
This article is licensed under a Creative Commons Attribution 3.0 Unported Licence.

At extended exposures (>48 h), PM_{150} in SLF resulted in a lengthening of the As–Fe distance consistent with ^{2}C coordination of amorphous ferric arsenate. *In silico* calculations indicate atomic coordination similar to the substitution of tetrahedral sulfate by arsenate in the T-Oh_3 jarosite structure in tridentate penta- and hexa-nuclear complexes.[91] The substitution of an arsenate tetrahedron (As–O_4 1.69 Å) into a sulfate tetrahedron site (S–O_4 1.54 Å) in the jarosite crystal system creates torsional and steric strain in the iron octahedral kagome lattice, decreasing the activation energy for breaking the As–O–Fe bonds, which may make arsenic from highly substituted jarosite more susceptible to release *in vivo* than from bidentate binuclear surface complexes at ferric (hydr)oxide surface sites.

Here, Fe XANES pre-edge combined with iron and arsenic EXAFS indicated that jarosite was the species most susceptible to SLF extraction. The lengthening of the 3.32 Å As–Fe bond in post SLF solids at 48 h further indicates a relative loss of the shorter As–Fe distance from As-loaded jarosite and/or accretion of arsenic complexed with ferric hydroxides. The affinity of arsenate for adsorption to ferric (hydr)oxide surfaces generates a surface complex that is relatively resistant to SLF IVBA. The high activity of phosphate in the SLF and sulfate from the dissolution of soluble salts (*e.g.*, gypsum) contributed competing ions that inhibited arsenic re-sorption, evidenced by S XANES showing increased loading of sulfate on ferrihydtite as the SLF reaction progressed, from 13% to 22% (Table S5†). The release of arsenic by SLF IVBA was parabolic, but not asymptotic, over the duration examined for lung fluid extractions in the PM_{10} and PM_{150} size range (Fig. 1), indicating more than one kinetic reaction rate, with an initial release dominated by dissolution of strained arsenic-substituted jarosite and secondary competing processes of solid phase repartitioning or precipitation under saturated conditions. It should be considered that the observed parabolic release may be due to accumulation of solutes in the closed IVBA batch system that would not develop in an open biosystem with continuously exchanging fresh biofluid. The release of arsenic from PM in SLF was not stoichiometric with iron. The ratio of Fe : As in unreacted PM_{10} and PM_{150} solids was 56.7 and 64.7, respectively. At the first SLF extraction step, the PM_{10} release was dominated by iron with respect to arsenic, 30 s Fe : As = 124, while PM_{150} showed diminished iron release relative to arsenic, Fe : As = 18.2 (Fig. 4). Both particle types showed an enrichment of arsenic release relative to iron release with increased reaction times, and the release of arsenic in both PM_{10} and PM_{150} to SLF approached unity (PM_{10} Fe : As_{100h} = 2.13, PM_{150} Fe : As_{100h} = 2.27) with extended incubations (Fig. 4). The Fe : As ratio in the solubilized (bioaccessible) pool decreased at each interval in PM_{10} and PM_{150} and fit to non-linear natural log of time curve (PM_{10} R^2 = 0.946, PM_{150} R^2 = 0.829) (Fig. 4). Where the molar ratio of Fe : As released to SLF was lower than the bulk ratio, *i.e.* after 15 minutes, for PM_{10} and over the duration of the IVBA experiment for PM_{150}, indicated that (i) dissolution of an arsenic enriched species, (ii) preferential arsenic release, or (iii) reprecipitation of iron were responsible for the solubilized species; and where the arsenic release exceeded iron it was seen as evidence that iron was precipitating as ferric (hydr)oxide without concurrent arsenic sorption.

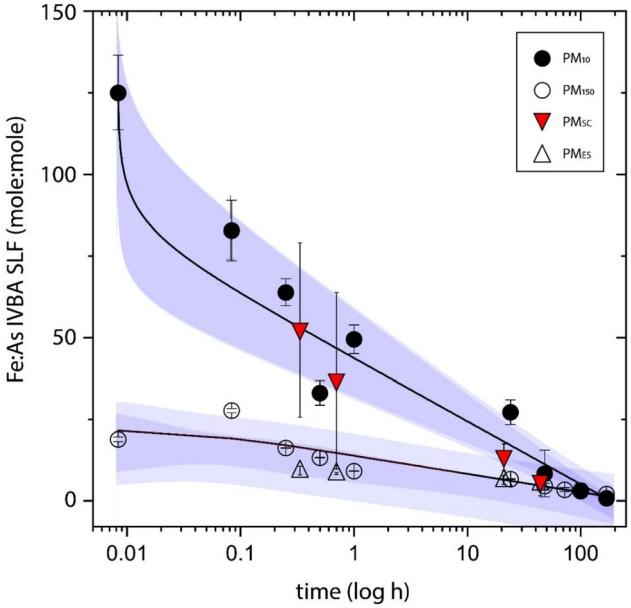

Fig. 4 Mole ratio of released iron and arsenic in SLF. Solid circles are PM_{10}, open circles are PM_{150}, closed downward red triangles are PM_{SC}, open triangles PM_{ES}, lines represent the best fit ($y = a - b*\ln(x + c)$) to the data, PM_{10} R^2 = 0.946, PM_{150}, R^2 = 0.829, fits to SC and ES not shown. Dark shaded bands represent the 95% confidence interval, light shading represents the 95% prediction band.

4.2 Lead speciation

4.2.1 SGF. The release of lead from PM_{10} to SGF increased with time to 100 h, and BAc reached a maximum of 18.2% (Fig. 1). The iron gastric IVBA followed a release curve very similar to lead (and arsenic), whereby it increased at each step to 100 h. The initial, a rapid, release of lead from the tailings was attributed to lead sequestered in acid soluble anglesite, which was released early in the reaction. Equilibrium modeling of anglesite solubility at the low pH and geochemical conditions of the SGF show a drive toward instability ($\log \Omega_{100h\text{-}SGF}$ = −17.1), which would release lead to gastric fluid.[92] Whereas equilibrium modeling showed the potential for precipitation of akaganeite, at the low pH of SGF Pb^{2+} sorption would be minimized and would not serve as a sink for lead. Further, because of the low phosphate activity and low pH, precipitation of pyromorphite as a sink for lead was not expected in SGF.[92,93] Lead released to the aqueous phase at extended reaction times could be limited by the stability of plumbojarosite (PM_{10}-$\log \Omega_{100h\text{-}SGF}$ = 10.9), for which the 100 h solution was supersaturated and could promote sequestration of lead (and iron) into the solid phase. The low pH SGF solution was not supersaturated with respect to any other lead minerals. Therefore, it is not expected that any neo-phase provided a sink for Pb^{2+} at extended exposures.

4.2.2 SLF. The maximum lead released in PM_{10} SLF occurred very quickly (less than 30 s), and the release at very short intervals suggests dissolution of a sulfate salt like anglesite ($PbSO_4$). The removal of lead from the aqueous phase after the initial pulse to SLF was attributed to supersaturation with respect to lead bearing apatite group minerals, *e.g.*

Open Access Article. Published on 03 ottobre 2022. Downloaded on 15/09/2024 20:54:19. This article is licensed under a Creative Commons Attribution 3.0 Unported Licence.

pyromorphite ([$Pb_5(PO_4)_3(Cl,OH)$], PM_{10} log $\Omega_{24h\text{-}SLF} = 6.9$) and subsequent precipitation. In the SLF, plumbo-jarosite [$Pb_{0.5}Fe_3(SO_4)_2(OH)_6$] precipitation was also predicted (PM_{10} log $\Omega_{24h} = 17.6$). Meanwhile, solutions were near equilibrium with respect to jarosite (PM_{10} log $\Omega_{24h} = 0.55$). The Fe : Pb ratio in unreacted PM_{10} solids was 98.0 (Table 1). The solubilized BAc Fe : Pb ratio ranged from 4.4–16 for all times through 100 h, indicating that the drive for dissolution and repartitioning of iron to the solid phase was much greater than for lead under high dissolved solids and circumneutral conditions of SLF. Lead XAS showed very little change in either XANES or EXAFS between unreacted and extended time points of SLF-reacted PM_{150} (Fig. S15 and Table S9†). The bioaccessible fraction of lead was very low, and spectroscopic evidence points to anglesite, a biofluid soluble lead-sulfate salt,[94] consistent with the observed kinetic lead release at seconds to minutes.[20] The potential inhalation risk to lead exposure from IK mine particles was greatest for the PM_{ES}, which had 100*x* lower total lead concentration compared to PM_{10} but released almost 68% in 48 h to SLF. The rapid-release of lead to SLF was likely due to the dissolution of anglesite, or lead (Pb^{2+}) substituted zinc (Zn^{2+}) sulfates. It has been shown that the BAc lead in mine tailings increases with increased weathering, where sulfides (galena, PbS) in the absence of excess PO_4^{3-} transform to plumbojarosite, and where pH conditions are not sufficiently low to promote the precipitation of plumbojarosite, anglesite forms as evaporative efflorescent salts and poses great inhalation hazard.[20,94] Efflorescent salts in and on mine tailings in dry climates may pose greater human health risk of lead exposure relative to humid environments precisely because of the enhanced formation of efflorescent salts and increased offsite transport of aerosols.[2] Specifically, the weathering of mine tailings in arid regions induces unique hydrogeochemically driven diagenetic alterations that impact the health risk of particulate exposures, attributed to evaporative deposition of lead-containing PM_{ES} at the surface.[15,20,94]

4.3 Iron and sulfur speciation

The risk associated with inhalation of PM, and subsequent exposure to arsenic and lead in the lungs from weathered sulfidic mine tailings, has been shown to be lower than gastric exposure at physiologically relevant time points of 1 h for SGF and 24 h for SLF. Further, health risks associated with arsenic PM exposure were mitigated, it seems, as arsenic BAc decreased with an increase in amorphous iron as ferrihydrite (Table 1). Iron release to the circumneutral pH and oxic conditions of SLF induces solution phase supersaturation with respect to ferrihydrite (PM_{150} log $\Omega_{24h} = 4.4$). The precipitation of ferrihydrite would provide fresh protonated surface sites ($\equiv FeOH_2^+$) for sorption of aqueous ions, *e.g.* oxyanion As^{5+} ($H_xAsO_4^{3-x}$, $pK_a^{x=1} = 6.96$). The strong affinity of arsenate for ferric hydroxide surfaces from neutral to acid pH can partially explain the low net release of arsenic to SLF, where arsenate forms inner-sphere bidentate binuclear complexes at ferric hydroxide surface sites.[95] Whereas ferrihydrite was not expected to precipitate in the low pH SGF (PM_{150} log $\Omega_{100\ h\text{-}SGF} = -2.28$), the modeled iron speciation of PM_{150} showed ferric hydroxy-chloride, similar to akaganeite (β-FeOOH), was supersaturated at long reaction timesteps in SGF. Precipitation of amorphous ferric hydroxides, inclusive of ferrihydrite and akaganeite, could scavenge oxyanions *in vitro*,[34] but would not sorb Pb^{2+} below pH 3.[96] Additionally, Fe XANES and EXAFS showed no evidence of increased ferric hydroxides in SGF at the longer residence time (Fig. 2). Second shell backscattering near neighbors of Fe–Fe in edge sharing coordination assigned to be associated with ferrihydrite showed a shortening of the Fe–Fe distance at 3.04 Å to 3.02 Å and 3.38 Å to 3.34 Å after 1 h in SGF. Longer distance contributions of Fe–Fe from corner sharing octahedra at 3.62 ± 2 Å showed a decrease in coordination from 2.3 to 1.0, and an insignificant increase in radial distance from 3.62 Å to 3.63 Å, and no change was observed from the contribution of Fe–S backscattering, but since no change was noted in the number of backscattering S atoms from 3.24 Å, dissolution of the jarosite component was not supported. An amorphous ferric arsenate structural model ('chain model') with Fe–Fe distances of about 3.6 Å has been proposed for sulfide mine waste environments and, if present, would partially explain the reduction in coordination of longer Fe–Fe 3.62 Å without a reduction in the Fe–S from jarosite.[97]

It was determined that the diminished soluble iron at the longest SLF exposures was due to *in vitro* artifact ferric solid precipitation. The PM_{10} was the particle of greatest inhalation risk to arsenic exposure, having both the highest total concentration and the greatest BAc release to SLF. The arsenic released to lung fluid for all particles (in decreasing concentration) was 2.1 μmol g^{-1} for PM_{10}, 0.76 μmol g^{-1} for PM_{150}, 0.16 μmol g^{-1} for PM_{SC} and 0.5 nmol g^{-1} $PM_{ES.}$ This becomes problematic as fine particles lodged in the lung could reside for days to years, and SLF IVBA showed increased risk to arsenic exposure from increased residence time *in vivo*. In addition to toxic response from arsenic and lead, oxidized iron particles can cause cell damage as they can act as electron shuttles (Fenton-like reactions) and produce oxidants and electrophiles that induce inflammation and oxidative stress.[98]

The high dissolved-salt and circumneutral environment of the SLF batch IVBA favored the precipitation of new solid species. Bioaccessibility release kinetics indicate that lead and iron partitioned back to the solid phase after an initial release to solution (Fig. 1), potentially as pyromorphite and hydrous ferric oxide. These precipitates had a lower affinity for arsenic than for lead, as indicated by the continued release of arsenic relative to lead over time. Hence, the low Pb_{SLF} release was attributed to *in vitro* formation of sparingly soluble pyromorphite (PM_{150} log $\Omega_{24h} = 7.7$). Sufficient excess PO_4^{3-} (1 mM) was present, not only to induce pyromorphite precipitation, but also to compete with dissolving $AsO4^{3-}{}_{(aq)}$ for newly generated surface hydroxyl sites of precipitating ferric (hydr)oxide, thereby promoting higher aqueous phase arsenic in SLF. Together with the high phosphate activity, competition from excess sulfate likely also inhibited arsenic re-adsorption.[99] Although PM_{150} metal(loid) bioaccessibility in SLF was low overall, the nature of PM dissolution incongruency affects As and Pb quite differently, such that these elements exhibit distinct patterns of net release

Open Access Article. Published on 03 ottobre 2022. Downloaded on 15/09/2024 20:54:19.
This article is licensed under a Creative Commons Attribution 3.0 Unported Licence.

that are strongly dependent on exposure time. While the back reactions promoted by supersaturation of sequestering solids may not be feasible *in vivo*, the mineralogy, speciation and solution chemistry should be evaluated as possible interferences *in vitro*.

In circumneutral lung fluid, at extended contact times (100 h), there was a thermodynamic drive for precipitation of ferrihydrite in SLF. However, as ferrihydrite formation can explain the decrease in aqueous iron activity; high phosphate and sulfate activity promoted ligand exchange and/or inhibited surface complexation of arsenate, resulting in increased arsenic released to lung fluid with each kinetic step from all particles studied. Because the release of arsenic from PM_{10} in lung fluid did not reach steady state during the IVBA, the potential slow release of lodged particles may present a long-term chronic health concern for particles with extended residence time. The risk associated with lead inhalation was greatest from efflorescent salts, while the total concentrations from PM_{ES} used here were relatively lower than other PM, the BAc was much greater. Conversely, the release of lead in SLF was attenuated with longer residence times, attributed to the precipitation of insoluble pyromorphite species.

At the Iron King site in AZ, the tailings have >0.2 wt% arsenic and lead, however analysis indicated that sequestration in jarosite reduced exposure risk of arsenic and lead from fine particles in low pH gastric fluid, consistent with recent findings.[39] The greatest deleterious health risks from ingestion of fugitive dusts were expected for the PM_{10}, which showed multi-metal(loid) enrichment, with arsenic and lead about 1.5*x* and 2.5*x* higher in PM_{10} compared to the bulk tailings (Table S10 and Fig. S17†). The acidic biogeochemical environment in SGF promotes the dissolution of ferrihydrite with concomitant releases of surface complexed arsenate from the PM. Whereas reprecipitation of ferrihydrite was not expected under acidic conditions (or in an open *in vivo* system), at long protracted exposures the IVBA solution becomes supersaturated with respect to plumbojarosite, which can sequester arsenate at up to 33% of the T sites.[100] The solid phase sequestration of lead at long exposures after 100 h was attributed to plumbojarosite and not precipitation of pyromorphite.

5 Conclusions

The research approach combined macroscopic studies of particle dissolution kinetics in synthetic lung and gastric biofluids with XAS of molecular speciation before, during, and after biofluid exposures. Speciation determination by XAS proved to be a powerful tool for determining molecular controls over arsenic and lead release to biofluids, and also provided key molecular-scale structural information pertaining to the host sulfate and ferric minerals in carrier dust PM.

The lead released from all PM in SLF approached an apparent maximum at ≤ 0.5 h, indicating that very short residence times in lung fluid pose important exposure risk, while the continued release of arsenic to SLF at each time step indicates longer exposures pose the greatest health risk. The greatest *in vitro* release from inhaled or ingestion fugitive dusts were expected from either metal(loid) containing soluble-efflorescent salts or PM_{10}. Along with particle size and specific surface area, arsenic and lead speciation exert control over their respective kinetic released to IVBA. Speciation was a function of the oxidative weathering of the initially deposited sulfides (arsenopyrite and galena) and the metal(loid) species associated with secondary minerals (jarosite and ferrihydrite) subsequently played a key role in toxin solubility and exposure *via* release in gastric and lung fluid.

The aim of a bioassay is to provide direct data estimates of human absorption of toxic metal(loid)s, and the established *in vitro* bioassay experiments are the best tools to achieve these heath and research aims. Further, it should be recognized that IVBA is effective for prediction of arsenic and lead bioaccessibility in a wide range of mine tailings and mine impacted soils.[101] Whereas IVBA it is not meant to model the entire complexity of the gastrointestinal tract in a simple bioassay, the limits of a closed batch system and lack of biosystem fluxes provides an incomplete representation speciation changes of ingested PM. Because the relative toxicity of particle-bound arsenic and lead depends on the bioavailability and *in vivo* speciation, which are impacted by the chemical forms ingested, *in vitro* bioassays cannot capture species dynamics in response to physiological systems (circulatory, urinary, *etc.*) where biochemical interactions can promote changes that can either increase or decrease the toxicity. Recent research implicates the gut microbiome in modulating metal(loid) toxicity, and the overall relationship between microbial activity and metal(loid) speciation, bioavailability, and toxicity is not currently understood.[102–104] Continued *in vitro* investigation, supported by limited and targeted *in vivo* experiments, will provide valuable information for determining health risk associated with fugitive dusts.

Author contribution

JC conceived the project and secured funding. RR and JC conceived and designed experiments. RR performed experiments and spectroscopic analysis. RR and JC wrote the manuscript.

Conflicts of interest

The authors declare no competing financial interest.

Acknowledgements

We acknowledge support from the National Institutes of Environmental Health Sciences SRP grant P42 ES04940. Portions of this research were carried out at Stanford Synchrotron Radiation Laboratory, a National User Facility operated by Stanford University on behalf of the U.S. Department of Energy, Office of Basic Energy Sciences. We acknowledge NASA grants NNX12AL47G and NNX15AJ22G and NSF grant 1531243 for funding of the instrumentation in the Kuiper Materials Imaging and Characterization Facility at the University of Arizona. We thank MaryKay Amistadi at ALEC for elemental analysis. We

Open Access Article. Published on 03 ottobre 2022. Downloaded on 15/09/2024 20:54:19.
This article is licensed under a Creative Commons Attribution 3.0 Unported Licence.

thank Steven Schuchardt, president of North American Industries, for providing access to the IKMHSS site. The authors declare they have no actual or potential competing financial interests.

References

1 K. Bradham, K. Scheckel, C. Nelson, P. Seales, G. Lee, M. Hughes, B. W. Miller, A. Yeow, T. Gilmore, S. M. Serda, S. Harper and D. J. Thomas, Relative bioavailability and bioaccessibility and speciation of arsenic in contaminated soils, *Environ. Health Perspect.*, 2011, **119**(11), 1629–1634.

2 J. Csavina, J. Field, M. P. Taylor, S. Gao, A. Landázuri, E. A. Betterton and A. E. Sáez, A review on the importance of metals and metalloids in atmospheric dust and aerosol from mining operations, *Sci. Total Environ.*, 2012, **433**, 58–73.

3 M. C. Corriveau, H. E. Jamieson, M. B. Parsons, J. L. Campbell and A. Lanzirotti, Direct characterization of airborne particles associated with arsenic-rich mine tailings: Particle size, mineralogy and texture, *Appl. Geochem.*, 2011, **26**(9–10), 1639–1648.

4 G. S. Plumlee and T. L. Ziegler. The medical geochemistry of dusts, soils, and other Earth materials, in, *Treatise on Geochemistry*, ed. Heinrich D. H., and Karl K. T., Oxford, Pergamon, 2007, p. 1–61.

5 J. Csavina, A. Landazuri, A. Wonaschutz, K. Rine, P. Rheinheimer, B. Barbaris, W. Conant, A. E. Sáez and E. A. Betterton, Metal and metalloid contaminants in atmospheric aerosols from mining operations, *Water, Air, Soil Pollut.*, 2011, **221**(1–4), 145–157.

6 A. L. Foster, R. P. Ashley and J. J. Rytuba, Arsenic species in weathering mine tailings and biogenic solids at the Lava Cap Mine Superfund Site, Nevada City, CA, *Geochem. Trans.*, 2011, **12**(1), 1–21.

7 M. J. Martínez-Sánchez, S. Martínez-López, L. B. Martínez-Martínez and C. Pérez-Sirvent, Importance of the oral arsenic bioaccessibility factor for characterising the risk associated with soil ingestion in a mining-influenced zone, *J. Environ. Manage.*, 2013, **116**, 10–17.

8 M. V. Ruby, R. Schoof, W. Brattin, M. Goldade, G. Post, M. Harnois, D. E. Mosby, S. W. Casteel, W. Berti, M. Carpenter, D. Edwards, D. Cragin and W. Chappell, Advances in evaluating the oral bioavailability of inorganics in soil for use in human health risk assessment, *Environ. Sci. Technol.*, 1999, **33**(21), 3697–3705.

9 R. Toujaguez, F. B. Ono, V. Martins, P. P. Cabrera, A. V. Blanco, J. Bundschuh and L. R. G. Guilherme, Arsenic bioaccessibility in gold mine tailings of Delita, Cuba, *J. Hazard. Mater.*, 2013, **262**, 1004–1013.

10 D. Craw and L. Pacheco, Mobilisation and bioavailability of arsenic around mesothermal gold deposits in a aemiarid environment, Otago, New Zealand, *Sci. World J.*, 2002, **2**, 308–319.

11 C. S. Kim, C. Chi, S. R. Miller, R. A. Rosales, E. S. Sugihara, J. Akau, J. J. Rytuba and S. M. Webb, (Micro)spectroscopic analyses of particle size dependence on arsenic distribution and speciation in mine wastes, *Environ. Sci. Technol.*, 2013, **47**, 8164–8171.

12 C. S. Kim, K. M. Wilson and J. J. Rytuba, Particle-size dependence on metal(loid) distributions in mine wastes: Implications for water contamination and human exposure, *Appl. Geochem.*, 2011, **26**, 484–495.

13 M. P. Taylor and K. A. Hudson-Edwards, The dispersal and storage of sediment-associated metals in an arid river system: The Leichhardt River, Mount Isa, Queensland, Australia, *Environ. Pollut.*, 2008, **152**(1), 193–204.

14 M. P. Taylor, A. K. Mackay, K. A. Hudson-Edwards and E. Holz, Soil Cd, Cu, Pb and Zn contaminants around Mount Isa City, Queensland, Australia: potential sources and risks to human health, *Appl. Geochem.*, 2010, **25**(6), 841–855.

15 R. A. Root, S. M. Hayes, C. M. Hammond, R. M. Maier and J. Chorover, Toxic metal(loid) speciation during weathering of iron sulfide mine tailings under semi-arid climate, *Appl. Geochem.*, 2015, **62**, 131–149.

16 M. O. Mendez and R. M. Maier, Phytostabilization of mine tailings in arid and semiarid environments - An emerging remediation technology, *Environ. Health Perspect.*, 2008, **116**, 278–283.

17 M. H. Mian and E. K. Yanful, Analysis of wind-driven resuspension of metal mine sludge in a tailings pond, *J. Environ. Eng. Sci.*, 2004, **3**(2), 119–135.

18 J. T. Overpeck and B. Udall, Climate change and the aridification of North America, *Proc. Natl. Acad. Sci.*, 2020, **117**(22), 11856–11858.

19 S. M. Hayes, P. A. O'Day, S. M. Webb, R. M. Maier and J. Chorover, Spectroscopic investigation of zinc speciation changes with pH in arid mine tailings in Aravaipa Canyon, Arizona, *Environ. Sci. Technol.*, 2011, **45**, 7168–7172.

20 S. M. Hayes, S. M. Webb, J. R. Bargar, P. A. O'Day, R. M. Maier and J. Chorover, Geochemical weathering increases lead bioaccessibility in semi-arid mine tailings, *Environ. Sci. Technol.*, 2012, **46**(11), 5834–5841.

21 T. Van de Wiele, C. M. Gallawa, K. M. Kubachka, J. T. Creed, N. T. Basta, E. A. Dayton, S. Whitacre, G. Du Laing and K. Bradham, Arsenic metabolism by human gut microbiota upon in vitro digestion of contaminated soils, *Environ. Health Perspect.*, 2010, **118**, 1004–1009.

22 M. R. Bailey, E. Ansoborlo, R. A. Guilmette and F. Paquet, Updating the ICRP human respiratory tract model, *Radiat. Prot. Dosim.*, 2007, **127**(1–4), 31–34.

23 G. S. Plumlee and S. A. Morman, Mine wastes: mine wastes and human health, *Elements*, 2011, **7**(6), 399–404.

24 P. B. Tchounwou, A. K. Patlolla and J. A. Centeno, Carcinogenic and systemic health effects associated with arsenic exposure - a critical review, *Toxicol. Pathol.*, 2003, **31**(6), 575–588.

25 E. Kenyon, W. Klimecki, H. El-Masri, R. Conolly, H. Clewel and B. Beck, How can biologically-based modeling of arsenic kinetics and dynamics inform the risk assessment process? — A workshop review, *Toxicol. Appl. Pharmacol.*, 2008, **232**(3), 359–368.

 This journal is © The Royal Society of Chemistry 2023

Open Access Article. Published on 03 ottobre 2022. Downloaded on 15/09/2024 20:54:19.
This article is licensed under a Creative Commons Attribution 3.0 Unported Licence.

26 A. Navas-Acien, E. K. Silbergeld, R. A. Streeter, J. M. Clark, T. A. Burke and E. Guallar, Arsenic exposure and type 2 diabetes: a systematic review of the experimental and epidemiologic evidence, *Environ. Health Perspect.*, 2006, **114**(5), 641–648.
27 C. J. Schmidlin, T. Zeng, P. Liu, Y. Wei, M. Dodson, E. Chapman and D. D. Zhang, Chronic arsenic exposure enhances metastatic potential via NRF2-mediated upregulation of SOX9, *Toxicol. Appl. Pharmacol.*, 2020, **402**, 115138.
28 M. Kampa and E. Castanas, Human health effects of air pollution, *Environ. Pollut.*, 2008, **151**(2), 362–367.
29 J. P. Bressler and G. W. Goldstein, Mechanisms of lead neurotoxicity, *Biochem. Pharmacol.*, 1991, **41**, 479–484.
30 M. J. Carroquino, M. Posada and P. J. Landrigan. Environmental Toxicology: Children at Risk, in, *Environmental Toxicology: Selected Entries from the Encyclopedia of Sustainability Science & Technology*, ed. Laws E. A., New York, NY, Springer New York, 2013. pp. 239–291.
31 S. J. Traina and V. Laperche, Contaminant bioavailability in soils, sediments, and aquatic environments, *Proc. Natl. Acad. Sci. U. S. A.*, 1999, **96**(7), 3365–3371.
32 S. W. Casteel, G. Fent, L. Myoungheon, W. J. Brattin and P. Hunter, *Relative Bioaccessibility of Arsenic in Two Soils from Iron King Mine*, prepared for US Environmental Protection Agency, Office of Superfund Remediation Technology Innovation, prepared by University of Missouri, Columbia and SRC, Report # SRC-09-041, 2010, http://semspub.epa.gov/src/document/09/2400040.
33 D. G. Beak, N. T. Basta, K. G. Scheckel and S. J. Traina, Bioaccessibility of arsenic(V) bound to ferrihydrite using a simulated gastrointestinal system, *Environ. Sci. Technol.*, 2006, **40**(4), 1364–1370.
34 C. Mikutta, P. N. Mandaliev, N. Mahler, T. Kotsev and R. Kretzschmar, Bioaccessibility of arsenic in mining-impacted circumneutral river floodplain soils, *Environ. Sci. Technol.*, 2014, **48**(22), 13468–13477.
35 L. Meunier, S. R. Walker, J. Wragg, M. B. Parsons, I. Koch, H. E. Jamieson and K. J. Reimer, Effects of soil composition and mineralogy on the bioaccessibility of arsenic from tailings and soil in gold mine districts of Nova Scotia, *Environ. Sci. Technol.*, 2010, **44**(7), 2667–2674.
36 M. V. Ruby, A. Davis, R. Schoof, S. Eberle and C. M. Sellstone, Estimation of lead and arsenic bioavailability using a physiologically based extraction test, *Environ. Sci. Technol.*, 1996, **30**, 422–430.
37 R. R. Karna, M. R. Noerpel, C. Nelson, B. Elek, K. Herbin-Davis, G. Diamond, K. Bradham, D. J. Thomas and K. G. Scheckel, Bioavailable soil Pb minimized by in situ transformation to plumbojarosite, *Proc. Natl. Acad. Sci.*, 2021, **118**(3), e2020315117.
38 F. Kastury, E. Smith, E. Doelsch, E. Lombi, M. Donnelley, P. L. Cmielewski, D. W. Parsons, K. G. Scheckel, D. Paterson, M. D. de Jonge, C. Herde and A. L. Juhasz, In vitro, in vivo, and spectroscopic assessment of lead exposure reduction via ingestion and inhalation pathways using phosphate and iron amendments, *Environ. Sci. Technol.*, 2019, **53**(17), 10329–10341.
39 T. D. Sowers, S. E. Bone, M. R. Noerpel, M. D. Blackmon, R. R. Karna, K. G. Scheckel, A. L. Juhasz, G. L. Diamond, D. J. Thomas and K. D. Bradham, Plumbojarosite remediation of soil affects lead speciation and elemental interactions in soil and in mice tissues, *Environ. Sci. Technol.*, 2021, **55**(23), 15950–15960.
40 S. M. Hayes, R. A. Root, N. Perdrial, R. M. Maier and J. Chorover, Surficial weathering of iron sulfide mine tailings under semi-arid climate, *Geochim. Cosmochim. Acta*, 2014, **141**, 240–257.
41 A. Valentín-Vargas, R. A. Root, J. W. Neilson, J. Chorover and R. M. Maier, Environmental factors influencing the structural dynamics of soil microbial communities during assisted phytostabilization of acid-generating mine tailings: A mesocosm experiment, *Sci. Total Environ.*, 2014, **500–501**, 314–324.
42 J. Gil-Loaiza, J. P. Field, S. A. White, J. Csavina, O. Felix, E. A. Betterton, A. E. Sáez and R. M. Maier, Phytoremediation reduces dust emissions from metal(loid)-contaminated mine tailings, *Environ. Sci. Technol.*, 2018, **52**(10), 5851–5858.
43 I. Manjón, M. D. Ramírez-Andreotta, A. E. Sáez, R. A. Root, J. Hild, M. K. Janes and A. Alexander-Ozinskas, Ingestion and inhalation of metal(loid)s through preschool gardening: An exposure and risk assessment in legacy mining communities, *Sci. Total Environ.*, 2020, **718**, 134639.
44 P. Gonzales, O. Felix, C. Alexander, E. Lutz, W. Ela and A. E. Sáez, Laboratory dust generation and size-dependent characterization of metal and metalloid-contaminated mine tailings deposits, *J. Hazard. Mater.*, 2014, **280**, 619–626.
45 A. N. Thomas, R. A. Root, R. C. Lantz, A. E. Sáez and J. Chorover, Oxidative weathering decreases bioaccessibility of toxic metal(loid)s in PM10 emissions from sulfide mine tailings, *GeoHealth*, 2018, **2**(4), 118–138.
46 N. T. Basta, and A. L. Juhasz. Using in vivo bioavailability and/or in vitro gastrointestinal bioaccessibility testing to adjust human exposure from soil ingestion, in *Geochemistry, Mineralogy and Microbiology of Arsenic in Environment. 79. Reviews in Mineralogy and Geochemistry*, ed. Bowell R. J., Majzlan J., and Alpers C. N., Mineralogical Society of America, 2014, ch. 9.
47 O. R. Moss, Simulants of lung interstitial fluid, *Health Phys.*, 1979, **36**(3), 447–448.
48 N. Menka, R. A. Root and J. Chorover, Bioaccessibility, release kinetics, and molecular speciation of arsenic and lead in geo-dusts from the Iron King Mine Federal Superfund site in Dewey-Humboldt, Arizona, *Rev. Environ. Health*, 2014, **9**(1–2), 23–27.
49 C. L. S. Wiseman, Analytical methods for assessing metal bioaccessibility in airborne particulate matter: A scoping review, *Anal. Chim. Acta*, 2015, **877**, 9–18.
50 N. M. Davies and M. R. Feddah, A novel method for assessing dissolution of aerosol inhaler products, *Int. J. Pharm.*, 2003, **255**(1–2), 175–187.

Open Access Article. Published on 03 ottobre 2022. Downloaded on 15/09/2024 20:54:19.
This article is licensed under a Creative Commons Attribution 3.0 Unported Licence.

51 C. Julien, P. Esperanza, M. Bruno and L. Y. Alleman, Development of an in vitro method to estimate lung bioaccessibility of metals from atmospheric particles, *J. Environ. Monit.*, 2011, **13**(3), 621–630.
52 H. Scholze and R. Conradt, An in vitro study of the chemical durability of siliceous fibres, *Ann. Occup. Hyg.*, 1987, **31**(4B), 683–692.
53 K. Koshi, Solubility and cell toxicity of cadmium, *Ind. Health*, 1979, **17**(3), 187–198.
54 E. K. Garger, A. A. Odintsov and A. D. Sazhenyuk, Estimation of the solubility of radioactive aaerosol particles in biological liquids, *Radiochemistry*, 2003, **45**(3), 298–303.
55 J. Wragg and B. Klinck, The bioaccessibility of lead from Welsh mine waste using a respiratory uptake test, *J. Environ. Sci. Health, Part A: Toxic/Hazard. Subst. Environ. Eng.*, 2007, **42**(9), 1223–1231.
56 J. W. Drexler and W. J. Brattin, An in vitro procedure for estimation of lead relative bioavailability: with validation, *Hum. Ecol. Risk Assess.*, 2007, **13**(2), 383–401.
57 A. L. Juhasz, P. Herde, C. Herde, J. Boland and E. Smith, Validation of the predictive capabilities of the Sbrc-G in vitro aassay for estimating arsenic relative bioavailability in contaminated soils, *Environ. Sci. Technol.*, 2014, **48**(21), 12962–12969.
58 H.-B. Li, M.-Y. Li, D. Zhao, J. Li, S.-W. Li, P. Xiang, A. L. Juhasz and L. Q. Ma, Arsenic, lead, and cadmium bioaccessibility in contaminated soils: measurements and validations, *Crit. Rev. Environ. Sci. Technol.*, 2020, **50**(13), 1303–1338.
59 K. D. Bradham, G. L. Diamond, K. G. Scheckel, M. F. Hughes, S. W. Casteel, B. W. Miller, J. M. Klotzbach, W. C. Thayer and D. J. Thomas, Mouse assay for determination of arsenic bioavailability in contaminated soils, *J. Toxicol. Environ. Health, Part A*, 2013, **76**(13), 815–826.
60 M. F. Hughes, V. Devesa, B. M. Adair, S. D. Conklin, J. T. Creed, M. Styblo, E. M. Kenyon and D. J. Thomas, Tissue dosimetry, metabolism and excretion of pentavalent and trivalent dimethylated arsenic in mice after oral administration, *Toxicol. Appl. Pharmacol.*, 2008, **227**(1), 26–35.
61 M. F. Hughes, V. Devesa, B. M. Adair, M. Styblo, E. M. Kenyon and D. J. Thomas, Tissue dosimetry, metabolism and excretion of pentavalent and trivalent monomethylated arsenic in mice after oral administration, *Toxicol. Appl. Pharmacol.*, 2005, **208**(2), 186–197.
62 M. F. Hughes, E. M. Kenyon, B. C. Edwards, C. T. Mitchell, L. M. Razo and D. J. Thomas, Accumulation and metabolism of arsenic in mice after repeated oral administration of arsenate, *Toxicol. Appl. Pharmacol.*, 2003, **191**(3), 202–210.
63 F. Hugenholtz and W. M. de Vos, Mouse models for human intestinal microbiota research: a critical evaluation, *Cell. Mol. Life Sci.*, 2018, **75**(1), 149–160.
64 H.-B. Li, M.-Y. Li, D. Zhao, J. Li, S.-W. Li, A. L. Juhasz, N. T. Basta, Y. M. Luo and L. Q. Ma, Oral bioavailability of As, Pb, and Cd in contaminated soils, dust, and foods based on animal bioassays: a review, *Environ. Sci. Technol.*, 2019, **53**(18), 10545–10559.
65 K. D. Bradham, G. L. Diamond, M. Burgess, A. Juhasz, J. M. Klotzbach, M. Maddaloni, C. Nelson, K. Scheckel, S. M. Serda, M. Stifelman and D. J. Thomas, In vivo and in vitro methods for evaluating soil arsenic bioavailability: relevant to human health risk assessment, *Journal of Toxicology and Eenvironmental Health*, 2018, **21**(2), 83–114.
66 USEPA, *Method 1340: In Vitro Bioaccessibility Assay for Lead in Soil*, SW-846, 2017, **https://www.epa.gov/sites/production/files/2017-03/documents/method_1340_update_vi_final_3-22-17.pdf**.
67 USEPA. *Validation Assessment of in Vitro Arsenic Bioaccessibility Assay for Predicting Relative Bioavailability of Arsenic in Soils and Soil-like Materials at Superfund Sites*, OLEM, 2017.
68 H.-B. Li, J. Li, A. L. Juhasz and L. Q. Ma, Correlation of in vivo relative bioavailability to in vitro bioaccessibility for arsenic in household dust from china and its implication for human exposure assessment, *Environ. Sci. Technol.*, 2014, **48**(23), 13652–13659.
69 M. Takaya, Y. Shinohara, F. Serita, M. Ono-Ogasawara, N. Otaki, T. Toya, A. Takata, K. Yoshida and N. Kohyama, Dissolution of functional materials and rare earth oxides into pseudo alveolar fluid, *Ind. Health*, 2006, **44**(4), 639–644.
70 A. G. Oomen, A. Hack, M. Minekus, E. Zeijdner, C. Cornelis, G. Schoeters, T. Van de Wiele, J. Wragg, C. J. Rompelberg, A. J. Sips and J. H. Van Wijnen, Comparison of five in vitro digestion models to study the bioaccessibility of soil contaminants, *Environmaental Science & Technology*, 2002, **36**(15), 3326–3334.
71 X. Hu, Y. Zhang, J. Luo, T. Wang, H. Lian and Z. Ding, Bioaccessibility and health risk of arsenic, mercury and other metals in urban street dusts from a mega-city, Nanjing, China, *Environ. Pollut.*, 2012, **159**(5), 1215–1221.
72 M. D. Ramirez-Andreotta, N. Lothrop, S. Wilkinson, R. Root, J. Artiola, W. Klimecki and M. Loh, Analyzing patterns of community interest at a legacy mining waste site to assess and inform environmental health literacy efforts, *Journal of Environmental Studies and Sciences*, 2015, 1–13.
73 M. D. Ramirez-Andreotta, M. L. Brusseau, P. Beamer and R. M. Maier. *Home gardening near a mining site in an arsenic-endemic region of Arizona: Assessing arsenic exposure dose and risk via ingestion of home garden vegetables, soils, and water Science of the Total Environment*. 2013;454–455:pp. 373–382.
74 X. Gao, R. A. Root, J. Farrell, W. Ela and J. Chorover, Effect of silicic acid on arsenate and arsenite retention mechanisms on 6-L ferrihydrite: A spectroscopic and batch adsorption approach, *Appl. Geochem.*, 2013, **38**, 110–120.
75 K. S. Savage, D. K. Bird and P. A. O'Day, Arsenic speciation in synthetic jarosite, *Chem. Geol.*, 2005, **215**, 473–498.

 This journal is © The Royal Society of Chemistry 2023

Open Access Article. Published on 03 ottobre 2022. Downloaded on 15/09/2024 20:54:19.
This article is licensed under a Creative Commons Attribution 3.0 Unported Licence.

76 J.-S. Youn, J. Csavina, K. P. Rine, T. Shingler, M. P. Taylor, A. E. Sáez, E. A. Betterton and A. Sorooshian, Hygroscopic properties and respiratory system deposition behavior of particulate matter emitted by mining and smelting operations, *Environ. Sci. Technol.*, 2016, **50**(21), 11706–11713.

77 A. R. Oller, M. Costa and G. Oberdörster, Carcinogenicity assessment of selected nickel compounds, *Toxicol. Appl. Pharmacol.*, 1997, **143**, 152–166.

78 S. Ganesan, A. T. Comstock and U. S. Sajjan, Barrier function of airway tract epithelium, *Tissue Barriers*, 2013, **1**(4), e24997.

79 M. Grafe, R. V. Tappero, M. A. Marcus and D. L. Sparks, Arsenic speciation in multiple metal environments: II. Micro-spectroscopic investigation of a CCA contaminated soil, *J. Colloid Interface Sci.*, 2008, **321**(1), 1–20.

80 D. Paktunc and J. E. Dutrizac, Characterization of arsenate-for-sulfate substitution in synthetic jarosite using X-ray diffraction and X-ray absorption spectroscopy, *Can. Mineral.*, 2003, **41**(4), 905–919.

81 K. S. Savage, D. K. Bird and P. A. O'Day, Arsenic speciation in synthetic jarosite, *Chem. Geol.*, 2005, **215**, 473–485.

82 A. L. Foster, G. E. Brown, T. N. Tingle and G. A. Parks, Quantitative arsenic speciation in mine tailings using X-ray absorption spectroscopy, *Am. Mineral.*, 1998, **83**, 553–568.

83 C. Mikutta, P. N. Mandaliev and R. Kretzschmar, New clues to the local atomic structure of short-range ordered ferric arsenate from extended X-ray absorption fine structure spectroscopy, *Environ. Sci. Technol.*, 2013, **47**(7), 3122–3131.

84 D. Paktunc, J. Dutrizac and V. Gertsman, Synthesis and phase transformations involving scorodite, ferric arsenate and arsenical ferrihydrite: Implications for arsenic mobility, *Geochim. Cosmochim. Acta*, 2008, **72**(11), 2649–2672.

85 F. B. Ono, R. Tappero, D. Sparks and L. R. G. Guilherme, Investigation of arsenic species in tailings and windblown dust from a gold mining area, *Environ. Sci. Pollut. Res.*, 2016, **23**(1), 638–647.

86 V. S. T. Ciminelli, D. C. Antônio, C. L. Caldeira, E. T. F. Freitas, I. D. Delbem, M. M. Fernandes, M. Gasparon and J. C. Ng, Low arsenic bioaccessibility by fixation in nanostructured iron (hydr)oxides: quantitative identification of As-bearing phases, *J. Hazard. Mater.*, 2018, **353**, 261–270.

87 W. Stumm, and J. J. Morgan, *Aquatic Chemistry: Chemical Equilibria and Rates in Natural Waters*, Hoboken, NJ, Wiley-Interscience, 1995.

88 W. Beckmann, *Crystallization: Basic Concepts and Industrial Applications*, Weinheim, Germany, Wiley-VCH, 2013.

89 R. Martin, K. Dowling, S. Nankervis, D. Pearce, S. Florentine and S. McKnight, In vitro assessment of arsenic mobility in historical mine waste dust using simulated lung fluid, *Environ. Geochem. Health*, 2018, **40**(3), 1037–1049.

90 S. Whitacre, N. Basta, B. Stevens, V. Hanley, R. Anderson and K. Scheckel, Modification of an existing in vitro method to predict relative bioavailable arsenic in soils, *Chemosphere*, 2017, **180**, 545–552.

91 J. Farrell, Tridentate arsenate complexation with ferric hydroxide and its effect on the kinetics of arsenate adsorption and desorption, *Chemosphere*, 2017, **184**, 1209–1214.

92 L. Xie and D. E. Giammar, Equilibrium solubility and dissolution rate of the lead phosphate chloropyromorphite, *Environ. Sci. Technol.*, 2007, **41**(23), 8050–8055.

93 G. Morin, J. Ostergren, F. Juillot, P. Ildefonse, G. Calas and G. E. J. Brown, XAFS determination of the chemical form of lead in smelter-contaminated soils and mine tailings: Importance of sorption processes, *Am. Mineral.*, 1999, **84**, 420–434.

94 S. M. Hayes, S. A. White, T. L. Thompson, R. M. Maier and J. Chorover, Changes in lead and zinc lability during weathering-induced acidification of desert mine tailings: Coupling chemical and micro-scale analyses, *Appl. Geochem.*, 2009, **24**(12), 2234–2245.

95 R. A. Root, S. Dixit, K. M. Campbell, A. D. Jew, J. G. Hering and P. A. O'Day, Arsenic sequestration by sorption processes in high-iron sediments, *Geochim. Cosmochim. Acta*, 2007, **71**(23), 5782–5803.

96 J. A. Dyer, P. Trivedi, N. C. Scrivner and D. L. Sparks, Lead sorption onto ferrihydrite. 2. Surface complexation modeling, *Environ. Sci. Technol.*, 2003, **37**(5), 915–922.

97 C. Mikutta, C. Schröder and F. M. Michel, Total X-ray scattering, EXAFS, and Mössbauer spectroscopy analyses of amorphous ferric arsenate and amorphous ferric phosphate, *Geochim. Cosmochim. Acta*, 2014, **140**, 708–719.

98 P. A. O'Day, A. Pattammattel, P. Aronstein, V. J. Leppert, and H. J. Forman, *Iron Speciation in Respirable Particulate Matter and Implications for Human Health*, Environmental Science & Technology, 2022.

99 P. Bose and A. Sharma, Role of iron in controlling speciation and mobilization of arsenic in subsurface environment, *Water Res.*, 2002, **36**(19), 4916–4926.

100 K. A. Hudson-Edwards, Uptake and release of arsenic and antimony in alunite-jarosite and beudantite group minerals, *Am. Mineral.*, 2019, **104**(5), 633–640.

101 E. Deshommes, R. Tardif, M. Edwards, S. Sauvé and M. Prévost, Experimental determination of the oral bioavailability and bioaccessibility of lead particles, *Chem. Cent. J.*, 2012, **6**(1), 138.

102 M. Coryell, M. McAlpine, N. V. Pinkham, T. McDermott and S. Walk, The gut microbiome is required for full protection against acute arsenic toxicity in mouse models, *Nat. Commun.*, 2018, **9**(1), 5424.

103 T. McDermott, J. Stolz and R. Oremland, Arsenic and the gastrointestinal tract microbiome, *Environ. Microbiol. Rep.*, 2019.

104 B. Roggenbeck, E. Leslie, S. Walk and E. Schmidt, Redox metabolism of ingested arsenic: Integrated activities of microbiome and host on toxicological outcomes, *Curr. Opin. Toxicol.*, 2019, **13**, 90–98.